Title: Sedimentary pyrite sulfur isotope compositions preserve signatures of the surface microbial mat environment in sediments underlying low-oxygen cyanobacterial mats

Running title: Pyrite sulfur isotope signatures in cyanobacterial mats

Author details and qualifications:

- Maya L. Gomes, PhD in Earth and Planetary Sciences from Northwestern University, current position: Assistant Professor, Johns Hopkins University
- Judith M. Klatt, PhD in Marine Microbiology from University of Bremen, current position: Research Scientist, Max Planck Institute for Marine Microbiology
- Gregory J. Dick, PhD in Marine Biology from Scripps Institution of Oceanography, University of California San Diego, current position: Associate Professor, University of Michigan
- Sharon L. Grim, PhD in Earth and Environmental Sciences from University of Michigan, current position: Postdoctoral Fellow, University of Michigan
- Kathryn I. Rico, PhD in Earth and Environmental Sciences from University of Michigan, current position: Postdoctoral Fellow, McGill University
- Matthew Medina, MS in Earth and Environmental Sciences from University of Michigan, current position: Artist
- Wiebke Ziebis, Doctorate in Geosciences, University of Bremen, Germany, current position: Associate Professor, University of Southern California
- Lauren Kinsman-Costello, PhD in Zoology and Ecology, Evolutionary Biology, and Behavior, Michigan State University, current position: Assistant Professor, Kent State University
- Nathan D. Sheldon, PhD in Geological Sciences, University of Oregon, current position: Professor, University of Michigan
- David A. Fike, PhD in Earth, Atmospheric and Planetary Sciences from Massachusetts Institute of Technology, current position: Professor, Washington University

This is the author manuscript accepted for publication and has undergone full peer review but has not been through the copyediting, typesetting, pagination and proofreading process, which may lead to differences between this version and the Version of Record. Please cite this article as doi: 10.1111/GBI.12466

Contact details for corresponding author: Maya Gomes
Department of Earth and Planetary Sciences
Johns Hopkins University, 127 Olin Hall
3400 N. Charles Street
Baltimore, MD 21218
Email: mgomes@jhu.edu
Phone: 410-516-3340

Acknowledgements and details of funding:
We thank the NOAA Thunder Bay National Marine Sanctuary Dive Unit – John Bright, Russ Green, Phil Hartmeyer, Wayne Lusardi, Stephanie Gandulla, Katie Clevenger, and Annie Wright – and R/V Storm Ship Captain Travis Smith for field support, site access, and sampling. We also thank Dirk de Beer, Arjun Chennu, Bopaiah Biddanda, Dack Stuart, Greg Druschel, Martin Kurek, Chase Howard, John Shukle, Hui Chien Tan, and Heidi Babos for help with field science operations and useful conversation and Stephanie Moore for laboratory and technical assistance. This work was supported by NSF grant EAR-1637066 to G.J.D. and W.Z., and a Washington University Environmental Studies Postdoctoral Research Fellowship to M.L.G.

DR. KATHRYN ISABEL RICO (Orcid ID : 0000-0003-2761-8663)
DR. NATHAN D SHELDON (Orcid ID : 0000-0003-3371-0036)

Article type : Original Article

Sedimentary pyrite sulfur isotope compositions preserve signatures of the surface microbial mat environment in sediments underlying low-oxygen cyanobacterial mats

Authors:
Maya L. Gomes[1*], Judith M. Klatt[2,3], Gregory J. Dick[3], Sharon L. Grim[3,4], Kathryn I. Rico[4,5], Matthew Medina[3], Wiebke Ziebis[6], Lauren Kinsman-Costello[7], Nathan D. Sheldon[3], David A. Fike[8]

Affiliations: [1]Department of Earth and Planetary Sciences, Johns Hopkins University, Baltimore, Maryland, USA; [2]Microsensor Group, Max Planck Institute for Marine Microbiology, Bremen Germany; [3]Department of Earth and Environmental Science, University of Michigan, Ann Arbor, Michigan, USA; [4]Exobiology Branch, National Aeronautics and Space Administration Ames Research Center, Mountain View, California, USA; [5]Department of Earth and Planetary Sciences, McGill University, Montreal, Quebec, Canada; [6]Department of Biological Sciences, University of Southern California, Los Angeles, California, USA; [7]Department of Biological Sciences, Kent State University, Kent, Ohio, USA; [8]Department of Earth and Planetary Sciences, Washington University, Saint Louis, Missouri, USA
* Corresponding author: Maya Gomes, Department of Earth and Planetary Sciences, Johns Hopkins University, 3400 N. Charles Street, Baltimore, MD 21218, Email: mgomes@jhu.edu.

Abstract

The sedimentary pyrite sulfur isotope ($\delta^{34}S$) record is an archive of ancient microbial sulfur cycling and environmental conditions. Interpretations of pyrite $\delta^{34}S$ signatures in sediments deposited in microbial mat ecosystems are based on studies of modern microbial mat porewater sulfide $\delta^{34}S$ geochemistry. Pyrite $\delta^{34}S$ values often capture $\delta^{34}S$ signatures of porewater sulfide at the location of pyrite formation. However, microbial mats are dynamic environments in which biogeochemical cycling shifts vertically on diurnal cycles. Therefore, there is a need to study how the location of pyrite formation impacts pyrite $\delta^{34}S$ patterns in these dynamic systems. Here we present diurnal porewater sulfide $\delta^{34}S$ trends and $\delta^{34}S$ values of pyrite and iron monosulfides from Middle Island Sinkhole, Lake Huron. The sediment water-interface of this sinkhole hosts a low-oxygen cyanobacterial mat ecosystem, which serves as a useful location to explore preservation of sedimentary pyrite $\delta^{34}S$ signatures in early Earth environments. Porewater sulfide $\delta^{34}S$ values vary by up to ~25‰ throughout the day due to light-driven changes in surface microbial community activity that propagate downwards, affecting porewater geochemistry as deep as 7.5 cm in the sediment. Progressive consumption of the sulfate reservoir drives $\delta^{34}S$ variability, instead of variations in average cell-specific sulfate reduction rates and/or sulfide oxidation at different depths in the sediment. The $\delta^{34}S$ values of pyrite are similar to porewater sulfide $\delta^{34}S$ values near the mat surface. We suggest that oxidative sulfur cycling and other microbial activity promotes pyrite formation in and immediately adjacent to the microbial mat and that iron geochemistry limits further pyrite formation with depth in the sediment. These results imply that primary $\delta^{34}S$ signatures of pyrite deposited in organic-rich, iron-poor microbial mat environments capture information about microbial sulfur cycling and environmental conditions at the mat surface and are only minimally affected by deeper sedimentary processes during early diagenesis.

1. Introduction

Sulfur isotope ($\delta^{34}S$) signatures of sedimentary pyrite deposited in Precambrian microbial mat environments have been used to investigate microbial sulfur cycling and environmental conditions during the early evolution of life (Wacey et al., 2010; Fischer et al., 2014; Meyer et al., 2017; Gomes et al., 2018). Geological evidence suggests that coastal environments and

possibly also the terrestrial realm were shaped by abundant microbial mats throughout Precambrian until the Neoproterozoic, which marks the decline of "matworld" and is linked with the appearance of complex eukaryotic life (Walter, 1976; Grotzinger and Knoll, 1999; Riding, 2006; Lenton and Daines, 2017; Peters et al., 2017). Microbial mat environments are multi-layered ecosystems composed of diverse microbial consortia, which host various types of photosynthetic, chemosynthetic, respiration, and fermentation reactions that drive rapid elemental cycling and shape geochemical gradients within the layers of the mat and the surrounding environment. Precambrian microbial mats likely represented hotspots for the evolution of new avenues of life due to steep physico-chemical gradients and were oases for intense local cycling of compounds that might have not undergone intense redox dynamics on a global scale, such as of sulfur (Des Marais, 2003). Microbial sulfate reduction (MSR) is among the most ancient metabolisms as inferred from isotope signatures, despite a much later onset of abundant sulfate supply to the oceans by weathering after the Great Oxidation Event (Lyons et al., 2009; Fike et al., 2015). Sulfur isotopes can record information about MSR, oxidative sulfur cycling, and environmental conditions and are thus particularly useful for investigating the history of biogeochemical cycling and how microbial mat ecosystems shaped Earth's redox evolution.

Pyrite $\delta^{34}S$ signatures in sediments deposited in microbial mat environments are often interpreted based on studies of sulfur isotope patterns in porewater sulfide ($\delta^{34}S_{sulfide}$) in modern microbial mats where there is accompanying information about microbial communities and environmental conditions (Habicht and Canfield, 1997; Fike et al., 2008; 2009; Gomes et al., 2020). These studies have shown that depth profiles of $\delta^{34}S_{sulfide}$ values can be explained by differential rates of metabolic activity operating at different depths in the mat, mostly involving microbially-mediated sulfate reduction, sulfide oxidation, and sulfur disproportionation processes. The $\delta^{34}S_{sulfide}$ patterns vary over diurnal cycles due to changes in light availability and microbial activity, and are also affected by sulfate levels (Fike et al., 2009).

A key question is if and how $\delta^{34}S$ signatures of pyrite (FeS_2, often extracted as the operationally-defined chromium reducible sulfide or CRS pool; Canfield et al., 1986) in microbial mats capture $\delta^{34}S_{sulfide}$ variability over diurnal cycles. In marine settings, $\delta^{34}S$ values of pyrite often reflect $\delta^{34}S_{sulfide}$ values at the location(s) of pyrite formation (Lyons, 1997). While it has been shown that pyrite $\delta^{34}S$ values are similar to porewater sulfide $\delta^{34}S$ values in sediments

underlying a cyanobacterial mat (Habicht and Canfield, 1997), the microbial mats that have been the subject of previous studies of diurnal trends in porewater $\delta^{34}S$ values lacked significant pyrite formation due to low reactive iron availability (Huerta-Diaz et al., 2011). This hinders our ability to determine how diurnal changes in sulfur cycling and the location(s) of pyrite formation in mats impact $\delta^{34}S$ signatures in pyrite deposited in microbial mat ecosystems.

Here we report $\delta^{34}S$ values of porewater sulfide and sequentially-extracted sedimentary sulfide mineral phases, including the acid-volatile sulfide fraction (primarily iron monosulfides; Rickard and Morse, 2005; Luther, 2005) and the CRS fraction that is operationally defined as sedimentary pyrite but may also include elemental sulfur (Canfield et al., 1986), in low-oxygen microbial mats in Middle Island Sinkhole (MIS), Lake Huron, USA. Low-oxygen conditions are a result of the combined influence of dense, oxygen-poor groundwater that enters through an alcove at the edge of the sinkhole and sinks to cover the mat-water interface and low rates of oxygen production via oxygenic photosynthesis (Biddanda et al., 2006; Ruberg et al., 2008; Biddanda and Weinke, accepted). In addition to being a useful site for studying geochemical records of sulfur cycling because pyrite is present in the sediments (Rico and Sheldon, 2019), MIS is also a valuable early Earth analog because it hosts low-oxygen cyanobacterial mats that were likely to be common in ancient, low-oxygen oceans (Grotzinger and Knoll, 1999; Dick et al., 2018). We show that $\delta^{34}S_{sulfide}$ patterns can be explained by progressive consumption of the sulfate reservoir. Diurnal changes in $^{34}S_{sulfide}$ patterns are driven by changes in net sulfate reduction at different depths in the sediment underlying the mat, which vary in response to light-driven changes in microbial communities and other taxa that affect porewater chemistry as deep as 7.5 cm within the sediment. Despite dynamic $\delta^{34}S_{sulfide}$ gradients, pyrite $\delta^{34}S$ values do not change significantly with depth and are similar to $\delta^{34}S_{sulfide}$ values recorded at the mat surface. These results, combined with previously published iron geochemistry data (Rico and Sheldon, 2019), indicate that pyrite primarily forms near the mat-water interface and captures $\delta^{34}S_{sulfide}$ signatures in the upper portions of the microbial mat. Surface microbial communities are likely to play a major role in promoting pyrite formation at the surface, and iron geochemistry (Rico and Sheldon, 2019) limits pyrite formation in deeper portions of the sediment. These results have implications for the interpretation of pyrite sulfur isotope records preserved in sediments deposited in ancient microbial mat environments.

1.1 Sedimentary sulfur isotope geochemistry

Sulfur isotope signatures in sedimentary pyrite record information about ancient sulfur cycling (Canfield and Farquhar, 2009; Fike et al., 2015). Sulfur isotopes are expressed in delta notation as permil (‰) deviations from an international standard ($\delta^{34}S$ = $\{[(^{34}S/^{32}S_{sample})/(^{34}S/^{32}S_{standard})]-1\}*1000$; where the standard is the Vienna Canyon Diablo Troilite or V-CDT). The dominant process that fractionates sulfur isotopes is MSR, where microorganisms use sulfate (SO_4^{2-}) to oxidize organic matter ('CH_2O'), producing bisulfide (H_2S), bicarbonate (HCO_3^-), and a hydrogen ion (H^+):

$$SO_4^{2-} + 2CH_2O \rightarrow HS^- + 2HCO_3^- + H^+ \quad \text{(eqn. 1)}$$

Sulfur isotope fractionation between sulfate and sulfide ($^{34}\varepsilon_{MSR} = \delta^{34}S_{sulfide} - \delta^{34}S_{sulfate}$) during MSR can be up to 70‰ and is commonly negatively correlated with cell-specific sulfate reduction rate (Harrison and Thode, 1958; Canfield et al., 2010; Sim et al., 2011; Leavitt et al., 2013). Thus, strain-specific relationships between cell-specific sulfate reduction rates and environmental conditions such as sulfate concentrations, mechanisms of sulfate transport across the cell membrane, organic carbon type and availability, and nutrient limitation and co-limitation impact $\delta^{34}S$ values of sulfate and sulfide (Bradley et al., 2016). Reservoir effects can also impact $\delta^{34}S$ values of sulfate and sulfide when sulfate levels are low and/or MSR is active in locations with limited system-openness (Jorgensen, 1979; Gomes and Hurtgen, 2013; 2015; Pasquier et al., 2017). The reservoir effect can be modeled as an irreversible reaction with a kinetic isotope effect occurring in a closed-system (i.e., Rayleigh fractionation; Mariotti et al., 1981) where the isotopic composition of the product approaches the isotopic composition of the initial reactant reservoir as the reactant reservoir is progressively consumed. Oxidative sulfur cycling reactions can also fractionate sulfur isotopes. However, magnitudes of these fractionations are generally low (~-7 to 5‰; see compilations in Zerkle et al., 2009; Gomes and Johnston, 2015; or Pellerin et al., 2019) compared to MSR, although fractionations of as low as -18‰ or as high as 18‰ have been reported at low pH (Kaplan and Rittenberg, 1964; Nakai and Jensen, 1964; Taylor et al., 1984) and for disproportionation reactions (Böttcher et al., 2001) or sulfide oxidation under alkaline conditions (Pellerin et al., 2019), respectively.

Sulfur isotope values of pyrite ($\delta^{34}S_{pyrite}$) capture isotopic signatures of ambient sulfide at the location of pyrite formation (e.g., at different locations in the sediment column or in the water column versus the sediment; Lyons, 1997) and therefore recorded values are not always representative of an entire system where they form. For example, it has been shown that $\delta^{34}S_{pyrite}$ values can differ from porewater sulfide $\delta^{34}S$ values by up to ~30‰, likely due to pyrite precipitation in biofilms utilizing sulfide that is the immediate product of sulfate reduction (Raven et al., 2016). Thus, information about both porewater sulfide and pyrite $\delta^{34}S$ patterns in modern microbial mats are particularly valuable for investigating what paleoenvironmental information is recorded in $\delta^{34}S_{pyrite}$ signatures in sediments deposited in microbial mat environments.

1.2 Pyrite formation

Relating the effects of microbial activity and environmental conditions on porewater $\delta^{34}S$ values to the pyrite $\delta^{34}S$ record requires accounting for the timing and location of pyrite formation and differentiating microbial impacts from post-depositional overprinting. Pyrite formation in natural systems is thought to occur through either the polysulfide (S_n^{-2}) pathway (eqn. 2, the Bunsen reaction) or the hydrogen sulfide (H_2S) pathway (eqn. 3, the Berzeluis reaction or Wächtershauser reaction; Rickard and Luther, 2007; Rickard, 2012):

$$FeS_{aq} + S_n^{-2} \rightarrow FeS_2 + S_{n-1}^{-2} \quad \text{(eqn. 2)}$$

$$FeS_{aq} + H_2S \rightarrow FeS_2 + H_2 \quad \text{(eqn. 3)}$$

Where FeS is iron monosulfide, which forms from the reaction of H_2S and Fe(II) in locations where pyrite formation is favorable (Rickard and Luther, 2007). Pyrite is the stable iron sulfide phase in Earth surface environments (Rickard and Luther, 2007; Rickard, 2012). However, pyrite formation is limited by the kinetic inhibition of pyrite nucleation, which requires supersaturated solutions (Schoonen and Barnes, 1991; Rickard and Luther, 2007; Rickard, 2012).

The mechanism that limits pyrite nucleation and therefore formation differs between the two pathways. For the polysulfide pathway (eqn. 2), high polysulfide concentrations increase rates of pyrite formation and thus the reaction between polysulfide and an iron species is the rate-controlling step (Rickard, 1975). For the hydrogen sulfide pathway (eqn. 3), the rate-controlling

step is the electron transfer between S(-II) and H(I) via an inner sphere complex between FeS and H_2S (Rickard and Luther, 1997; Ricard, 1997). More broadly, it is thought that microbes can play a role in promoting pyrite formation – via direct effects on precipitation (Thiel et al., 2019) or due to templating on cell walls or other organic substrates (Donald and Southam, 1999; Rickard et al., 2007). Conversely, some types of organic matter can hinder pyrite formation (e.g., aldehydic carbonyls; Rickard et al., 2001). These studies provide insights into why pyrite formation often occurs near the transition to sulfidic waters in modern systems; for example, sedimentary pyrite in the Black Sea captures the $\delta^{34}S$ signature of sulfide at the top of the zone of sulfate reduction, which occurs in the water column, rather than deeper in the water column and/or sediment (Lyons, 1997). Reactants involved in the rate-limiting steps (i.e., S_n^{-2}, H_2S, and FeS_{aq}) are stable and/or formed by microbial activity in these locations, resulting in supersaturated conditions that promote pyrite nucleation and formation (Rickard and Luther, 2007; Rickard, 2012). These steep geochemical gradients occur in microbial mats and shift over diurnal cycles (e.g., Fike et al., 2008; 2009). Thus, knowledge of how these gradients shape $\delta^{34}S_{pyrite}$ signatures will improve our ability to use the geological record to investigate the coupled evolution of life and the Earth surface.

2. Methods

2.1 Study Site

A modern analog for Proterozoic cyanobacterial mats with pyrite formation can be found in Middle Island Sinkhole (MIS), MI, USA (45° 11.914 N, 83° 19.671 W; Figure 1). MIS is a submerged depression in Lake Huron formed by the collapse of Devonian aged carbonates of the Traverse group. The ~10,000 m^2 depression lies ~13 m below the surrounding lake floor at a water depth of 23 m (Biddanda et al., 2006; Ruberg et al., 2008) and is overlain by high-conductivity water (specific conductivity of ~2300 $\mu s\ cm^{-1}$) that emerges from a seep (termed the alcove) located in the south-east edge of the sinkhole (Biddanda et al., 2006; Ruberg et al., 2008). The ionic strength of the water arises from dissolution of salts due to reactions between groundwater and limestones and evaporites from the Middle Devonian Detroit River Group that underlies the Traverse group (Biddanda et al., 2006; Ruberg et al., 2008). Density stratification

inhibits mixing with the overlying water, resulting in low-oxygen (~2-4 mg L^{-1}) waters overlying the sediment-water interface (SWI; Ruberg et al., 2008). Light penetration to the SWI supports a dynamic microbial mat ecosystem (Biddanda et al., 2006; 2015; Nold et al., 2010a; Voorhies et al., 2012; 2016; Snider et al., 2017; Kinsman-Costello et al., 2017; Grim, 2019).

Much of the SWI of the flat, deep portion of the sinkhole is covered with ~2 mm-thick purple mats dominated by cyanobacterial groups taxonomically similar to Phormidium and Planktothrix (Nold et al., 2010a; Voorhies et al., 2012; 2016). Patches of white, filamentous sulfide-oxidizing bacteria, such as Beggiatoa or Epsilonproteobacteria, are also variably present at the SWI (Biddanda et al., 2006; 2015; Nold et al., 2010a; Voorhies et al., 2012). Both the purple cyanobacteria and the white filamentous bacteria are capable of vertical migration and therefore the surface appearance of the mat can change over diurnal cycles (Nold et al., 2010a; Voorhies et al., 2012; Biddanda et al., 2015). Deltaproteobacteria, including various potential sulfate reducers, are abundant within the mat and underlying sediment (Kinsman-Costello et al., 2017). Eukaryotic taxa identified in the mats by 18S rRNA gene surveys include ciliates, nematodes, and tardigrades (Nold et al., 2010b). Microscopy confirmed the presence of many of these eukaryotic taxa, as well as diatoms (Merz et al., 2020).

Sediment underlying the ~2 mm-thick microbial mats is different than the surrounding Lake Huron sediment (Nold et al., 2013; Rico and Sheldon, 2019; Rico et al., 2020). Carbon isotope signatures in the sedimentary organic matter underlying the mats indicate that it is sourced from settling phytoplankton (Nold et al., 2013; Rico and Sheldon, 2019; Rico et al., 2020), and some trace metals like molybdenum show modest enrichments due to particulate shuttling (Rico et al., 2019). Overall, the MIS sediments have higher total organic carbon, iron, and trace metal concentrations than Lake Huron sediments due to differences in redox chemistry and geomicrobiological conditions between the sinkhole and surrounding environment (Nold et al., 2013; Rico and Sheldon, 2019; Rico et al., 2019; 2020).

2.2 Sampling

Sampling, in situ deployments, site characterization, and site photography were carried out by SCUBA divers from The Thunder Bay National Marine Sanctuary Dive Unit. Sediment cores were hand-collected using plexiglass tubes that were inserted into the sediment and then sealed

with rubber stoppers before extraction. The cores were used to assess (1) sulfate reduction rates and porewater sulfate concentrations, (2) porewater sulfide, pH, and dissolved oxygen dynamics using microsensors under controlled laboratory conditions, and (3) sulfur isotope compositions of solid-phase sulfides. In situ deployments of black and white photo film were used to capture diurnal $\delta^{34}S_{sulfide}$ patterns in the porewater (Fike et al., 2017). Water emerging from the alcove was sampled by a peristaltic pump for (1) analysis of sulfate $\delta^{34}S$ values and (2) use in ex situ microsensor measurements. In situ deployments, water sampling for sulfate $\delta^{34}S$ analysis, and core collection for sulfate reduction rate and porewater sulfate concentration measurements were performed over the course of a 2-week field campaign in July 2016. Cores for solid-phase sulfide sulfur isotope geochemistry were sampled in 2015. Cores and water for ex situ microsensor measurements were collected in May 2017.

2.3 Sulfate reduction rates and porewater sulfate concentrations

Two sediment cores for porewater sulfate concentration and five sediment cores (ID 2.5 cm) for sulfate reduction rate measurements were obtained from locations covered with purple mat (near node A0 in Figure 1). Cores were transported upright and in the dark back to land, where incubations were done the same day that the cores were collected.

Sulfate reduction rates were measured according to the whole-core injection method (Jørgensen, 1978). Radio-labeled sulfate (200 KBq $^{35}SO_4$ dissolved in 6 µl water) was injected in 1-cm depth intervals. After injection, cores were incubated in a water bath at in situ temperature (~9° C) in the dark for 20 minutes. After incubation, cores were sectioned at 1-cm intervals. Sulfate reduction was stopped by transferring core sections immediately into 10 ml of ice-cold 20% zinc acetate. Sulfate reduction rates were determined using the cold chromium distillation for radiolabeled sulfide (Fossing & Jørgensen 1989, Kallmeyer et al. 2004).

Porewater from a separate set of two cores was obtained by centrifugation of 1 cm sediment sections and subsequent filtration of the supernatant with 0.45 µm PES syringe filters. Samples were flash frozen in liquid butane and kept frozen until analysis. Sulfate concentration in the porewater was determined by membrane-suppression ion chromatography (Dionex, Thermo Scientific). Uncertainty of sulfate concentration analyses is <2%, determined as the relative standard deviation of check standards.

2.4 Ex-situ microsensor measurements

Cores (ID 10 cm) with purple mat and water taken between nodes A1, A2, B1, and B2 in Figure 1 were transported to the laboratory in Ann Arbor, MI upright, in the dark, and cooled. During measurements, the core was kept at 14°C and the water column was covered with paraffin oil to prevent exchange with air. The water column was fed with MIS bottom water using a peristaltic pump from a thermostated recycling reservoir to adjust a gentle flow across the mat-water interface and purged with N_2-air mixtures to adjust oxygen concentration. Light was supplied from a halogen light source (Schott). Light intensity was assessed with a cosine-corrected quantum sensor connected to a light meter (both LiCor).

Microsensors for dissolved oxygen (O_2), H_2S, and pH determination were built, calibrated and used as described previously (Revsbech, 1989; Jeroschewski et al., 1996; de Beer et al., 1997). Uncertainty of these measurements are ±12% for O_2, ±3% for H_2S, and ±0.1% for pH. Total sulfide concentrations ($\Sigma[S^{2-}]$, $[HS^-]$, $[H_2S]$, where brackets denote concentration) were calculated from the H_2S and pH profiles using a pK_a of 7.16. Profiles were measured under different light and dissolved oxygen levels to examine if dynamics in pH, O_2, and sulfide concentration could be explained by the presence of cable bacteria (e.g., Nielsen et al., 2010; Pfeffer et al., 2012; Seitaj et al., 2015). Conditions were: (1) light (58 µmol photons m^{-2} s^{-1}) to mimic mid-day light conditions at MIS (cf., Merz et al., 2020) and ~130 µM O_2 and (2) dark (<0.5 µmol photons m^{-2} s^{-1}) and ~13 µM O_2 in the overlying water column. Profiles under both conditions (light and dark, low O_2) were measured in the same spot over the course of ~1 hour – time scales that are sufficiently long to differentiate the impact of cable bacteria versus diffusion on chemical profiles (e.g., Nielsen et al., 2010), but sufficiently short that processes related to cm-scale migration of diatoms and other diurnally varying processes should not affect pH, O_2, and sulfide trends (Merz et al., 2020).

2.5 Deployments for porewater sulfide sulfur isotope geochemistry

Black and white photo film (Ilford Delta 100 Professional) was used to capture 2D patterns of porewater sulfide sulfur isotope geochemistry by reaction between porewater sulfide and

309 silver within the film, forming silver sulfide (Fike et al., 2017). Over a period of three days (July
310 21-23, 2016), the films were deployed for 2.5-5.5 hours at four time intervals to explore changes
311 in porewater sulfide $\delta^{34}S$ values over diurnal cycles (Table 1): morning (9:30-13:30), afternoon
312 (15:00-17:30), evening (16:30-22:00), and night (22:15-2:45). The films were deployed at
313 locations (Figure 1) with two different surface characteristics: (1) sediment covered with purple
314 microbial mat during the day and white mat at night, hereafter termed the purple mat (located
315 near nodes B4 and B5 in Figure 1; image of a deployed film shown in Figure 2A) and (2) grey
316 sediment lacking visible cohesive mat at the surface with white material variably present (located
317 near node B2 in Figure 1; image of a deployed film shown in Figure 2B), hereafter termed the
318 grey mat. In total, 8 films were deployed (i.e., four time intervals at two sites). Pictures of
319 deployed films were taken at the beginning and end of each deployment. After retrieval, films
320 were removed from sunlight, rinsed, and allowed to dry before storage in the dark. Images of
321 deployed films and appearance after removal, rinsing, and drying are shown in Figures S1-S8 in
322 the supplemental materials.
323 Sulfide was extracted from film sections cut at 1 cm intervals by boiling in 6N hydrochloric
324 acid for 2 hours in an anoxic reaction vessel. The hydrogen sulfide gas released by the reaction
325 was driven via a N_2 carrier gas through a citric acid and sodium citrate buffered water trap (pH =
326 4) into a trap vessel with 1M silver nitrate to precipitate the sulfide as silver sulfide. The silver
327 sulfide was purified by rinsing with 1M ammonium hydroxide solution and rinsed three times
328 with deionized water. Sulfide yields from films were determined gravimetrically.
329 Silver sulfide samples were mixed with vanadium pentoxide and combusted to SO_2 for sulfur
330 isotope analysis on a Costech Elemental Analyzer coupled to a DeltaV Isotope ratio mass
331 spectrometer at Washington University. S isotope measurements were reproducible within 0.2‰
332 based on repeat analysis of international standards (IAEA S-1 and IAEA S-3) and the
333 Washington University in-house Ag_2S, $BaSO_4$, and ZnS standards. All porewater sulfide $\delta^{34}S$
334 data was corrected to account for the small (1.2 ± 0.5 ‰) known offset between aqueous sulfide
335 and sulfide trapped in photo films associated with sulfide diffusion into the film and the reaction
336 with silver to form Ag_2S (Fike et al., 2017).
337
338 2.6 Solid-phase sulfide sulfur isotope geochemistry
339

Two sediment cores were used for solid-phase sulfide $\delta^{34}S$ analysis (location near node C3 in Figure 1). No specific mat types were targeted for core extraction because the appearance of mats at the sediment-water interface varies from year to year and sediment geochemistry is time-averaged. Sediment geochemistry was preserved by placing the cores on dry ice; cores were transported frozen to the University of Michigan in Ann Arbor, MI, where they were stored at −20 °C. Frozen cores were sectioned via table saw according to depth (three 1 cm sections at the top, then 3 cm downcore). Sections were freeze-dried and homogenized prior to analysis.

A sequential procedure was used to extract operationally defined pools of sedimentary sulfide: (1) acid-volatile sulfide (AVS), which is predominantly iron monosulfides (Chanton and Martens, 1985), and (2) chromium-reducible sulfide (CRS), which recovers pyrite and elemental sulfur (Canfield et al., 1986). Sediment was placed in reaction vessels, which were purged of oxygen using N_2 gas. The AVS was first extracted by boiling in 6N HCl for 2 hours (Chanton and Martens, 1985) and the CRS was then extracted by boiling the residual sediment with acidified chromium (II) chloride solution for 2 hours (Canfield et al., 1986). For both AVS and CRS extractions, the liberated hydrogen sulfide was driven via a N_2 carrier gas through a citric acid and sodium citrate buffered water (pH = 4) into the silver nitrate solution filled trap vessel to trap the sulfide as silver sulfide. The silver sulfide was purified, rinsed, and analyzed for $\delta^{34}S$ values as previously described in section 2.5.

The sequential extraction procedure was done on samples that had been previously freeze-dried, homogenized, and stored under ambient atmospheric conditions. It is likely that some components of the AVS pool may have been lost during sample handing, nonetheless the sequential extraction procedure was performed in order to preclude mixing of the CRS and AVS pools. It is unlikely that the storage conditions impacted sulfur isotope signatures of CRS because fractionations associated with abiotic oxidation of pyrite in the presence of oxygen are low (<1‰; Balci et al., 2007).

2.7 Sulfate sulfur isotope geochemistry

Alcove water samples were treated with 3% zinc acetate solution in the field to trap any sulfide as zinc sulfide. After transport back to the lab, the samples were filtered at 0.45 μm to remove zinc sulfide and any other particulates. Saturated barium chloride solution was added to

the filtered samples to precipitate sulfate as barium sulfate. Purification of the barium sulfate was done using the diethylenetriaminepentaacetic acid dissolution and reprecipitation procedure (D-DARP; Bao, 2006). Barium sulfate samples were mixed with vanadium pentoxide and $\delta^{34}S$ values were determined as described in section 2.3.

3. Results

3.1 Site conditions

In July 2016, much of the sediment-water interface (SWI) of the Middle Island Sinkhole (MIS) was dominated with surface coverings that were similar to those described in previous studies (Biddanda et al., 2006; 2015; Ruberg et al., 2008; Nold et al., 2010a; 2013; Voorhies et al., 2012; Snider et al., 2017; Kinsman-Costello et al., 2017): purple mats, grey sediment lacking cohesive mat, and intermittently observed white patches. We chose to focus on the two most commonly observed surface coverings to study diurnal $\delta^{34}S$ patterns in porewater sulfide in 2016: the purple mats and grey sediment with diffuse mat at the SWI (i.e., grey mats) as two common end-member environments (Figure 2). The thickness of the purple mat was ~2 mm. The diffuse grey mat lacked a substantial cohesive mat layer at the surface (Figure 2).

3.2 Sulfate reduction rates and porewater sulfate concentrations

Sulfate reduction rates in the sediment underlying the purple mat (Figure 3; Table S1) are highest just below the SWI at 0.5 cm (mean = 1803.7 nmol cm^{-3} d^{-1}, σ = 896.8 nmol cm^{-3} d^{-1}; n = 5) and decrease to low and variable values deeper in the sediment (between ~25 and ~835 nmol cm^{-3} d^{-1}, with one potential outlying value of 1707.7 nmol cm^{-3} d^{-1} at 5.5 cm). There is a second peak in sulfate reduction rates at 5.5 cm, consistent with the concave shape of the concentration depth profiles (Figure 3). The mean sulfate reduction rate at this depth was 841.6 nmol cm^{-3} d^{-1} (σ = 502.6 nmol cm^{-3} d^{-1}; n = 5) or 625.1 nmol cm^{-3} d^{-1} (σ = 156.0 nmol cm^{-3} d^{-1}; n = 4) if the potential outlier is removed. However, given that the increase in sulfate reduction rate is not defined by one point and is reproducible in all five cores, it is not likely to be an analytical artifact and therefore may be representative of the natural variability in the system. Sulfate

concentrations decreased from 5.3 ± 0.2 mM at 0.5 cm to 0.1 ± 0.03 mM at 9.5 cm (Figure 3; Table S1). There was a slight increase in sulfate concentrations to 0.6 ± 0.5 mM at 10.5 cm before sulfate concentrations continue to decrease to 0.5 ± 0.6 mM at 11.5 cm (although this deep sulfate concentration variability was only observed in one porewater profile).

3.3 Ex situ microsensor measurements of O_2, pH, and sulfide

Ex situ microsensor measurements were done on purple mat and underlying sediments under illumination mimicking mid-day light conditions at MIS (58 µmol photons m^{-2} s^{-1}; Merz et al., 2020; Biddanda and Weinke, accepted). Concentrations of O_2 were ~125 uM in the overlying water, peaked at 271.4 uM at 0.5 mm in the mat, decreased to undetectable levels by 2 mm, and remained undetectable in the sediment underlying the mat (Figure 4; Table S2). Sulfide was undetectable in the mat and started to increase at 2.75 mm, reaching a maximum of 5.1 mM in the deepest measurements (48.5; Figure 4; Table S2). A peak in pH (8.2) occurred at 0.5mm in the mat overlapping with the O_2 peak, consistent with photosynthetic O_2 production (e.g., Revsbech et al., 1983). The pH peak was followed by a rapid decline to 7.3 at 1.25 mm in the zone of O_2 and sulfide consumption, suggesting aerobic sulfide oxidation to sulfate (Klatt and Polerecky, 2015). Below the mat, pH gradually increased to ~7.7 in the deepest measurements (48.5 mm; Figure 4; Table S2). Upon darkening and adjustment of water column O_2 concentrations to ~13 µM, the photosynthetic O_2 concentration and pH peak disappeared and the zone of aerobic sulfide oxidation moved to the uppermost 0.5 mm. Changes in the light regime and O_2 concentration in the water column over ~30 mins to 1 hour did not affect the concentration profiles beyond the uppermost 3 mm.

3.4 Sulfur isotope patterns

Porewater sulfide was recovered using photo film (Fike et al., 2017) from all analyzed depth intervals at all times of day except for the uppermost sample (0.5 cm) from the purple mat in the afternoon. All of the porewater sulfide sulfur isotope ($\delta^{34}S_{sulfide}$) profiles show similar patterns (Figure 5; Table S3): $\delta^{34}S_{sulfide}$ values were low (-7.1 to 11.1‰) near the SWI relative to deeper portions of the mat, where $\delta^{34}S_{sulfide}$ values stabilized at ~15 to 18‰ with maximum values

reached at ~1 to 8 cm below the mat surface (Figure 5; Table S3). The deep $\delta^{34}S_{sulfide}$ values (~15 to 18‰) were slightly lower than $\delta^{34}S_{sulfate}$ in the alcove water, which had an average $\delta^{34}S$ value of 18.9‰ (σ = 0.16‰; n = 4).

The magnitude of surface porewater sulfide ^{34}S-depletion and the depth where $\delta^{34}S_{sulfide}$ values approach $\delta^{34}S_{sulfate}$ values varied with time of day and between the purple and grey mats. In the purple mat, night and morning $\delta^{34}S_{sulfide}$ patterns were similar (Figure 5; Table S3). In the afternoon, sulfide levels were too low at 0.5 cm to measure $\delta^{34}S_{sulfide}$ values. The depth where $\delta^{34}S_{sulfide}$ values approached their maximum also gets lower in the afternoon reaching ~15‰ only at 7.5 cm. In the evening, the $\delta^{34}S_{sulfide}$ profile was ^{34}S-enriched compared to other times in the day, with a $\delta^{34}S_{sulfide}$ value of 11.1‰ at 0.5 cm and approaching maximum values at 1.5 cm. In the grey diffuse mat, $\delta^{34}S_{sulfide}$ values were generally higher at the surface compared to purple mat and the depth at which values reach their maximum was less dynamic. Maximum values were approached at 4.5 cm in the evening, night and morning (Figure 5; Table S3). In the evening, $\delta^{34}S_{sulfide}$ values in the surface were slightly enriched compared to night and morning (3.5‰ vs ~2‰). In the afternoon, the $\delta^{34}S_{sulfide}$ profiles were the most ^{34}S-enriched, with a $\delta^{34}S_{sulfide}$ value of 11.0‰ below the SWI (0.5 cm) increasing to high values (~15-16‰) at 1.5 cm.

Sequentially extracted sedimentary sulfides include the operationally defined pools of acid-volatile sulfide (AVS; primarily composed of iron monosulfides) and chromium-reducible sulfide (CRS; primarily composed of pyrite and elemental sulfur). Due to sample drying prior to the sequential extraction procedure and storage at ambient atmospheric conditions, it is likely that some component of the AVS was lost. In many of the samples, especially deep (>10.5 cm) samples, there was insufficient recovery of AVS for $\delta^{34}S_{AVS}$ analyses.

Similar to the $\delta^{34}S_{sulfide}$ patterns, $\delta^{34}S_{AVS}$ values were lowest near the SWI and became ^{34}S-enriched with depth (Figure 6; Table S4). In the October core, $\delta^{34}S_{AVS}$ values were – 0.3‰ at the surface, increased to 9.9‰ at 2.5 cm, and then decreased slightly to 7.8‰ at 10.5 cm. In the July core, $\delta^{34}S_{AVS}$ values ranged between -7.3‰ and -3.4‰ in the top 3 cm and then became higher but also quite variable, reaching a value of 18.5‰ at 7.5 cm before decreasing to 5.7‰ at 10.5 cm. CRS showed the smallest amount of $\delta^{34}S$ variability; $\delta^{34}S_{CRS}$ values ranged from ~-10 to 1‰ in both the July and October 2015 cores. There was a slight pattern of ^{34}S-enrichment with depth

463 in both cores, but $\delta^{34}S_{CRS}$ values never reached the high $\delta^{34}S$ values in porewater sulfide (~15 to
464 18‰) measured from deeper sediments (>5 cm below SWI).
465
466 4. Discussion
467
468 4.1 Diurnal trends in porewater sulfide
469
470 Profiles in both purple and grey mats at Middle Island Sinkhole (MIS) show similar trends of
471 low porewater $\delta^{34}S_{sulfide}$ values (-7.1 to 11.1‰) at the sediment water interface (SWI) that
472 increase with depth as the sulfate reservoir is progressively consumed (Figures 3 and 5).
473 Consumption of the sulfate reservoir by MSR is consistent with previously measured porewater
474 sulfate and sulfide concentration profiles (Kinsman-Costello et al., 2017). These concentration
475 and isotope patterns are often attributed to Rayleigh isotope fractionation under closed system
476 conditions (e.g., Jorgensen, 1979). In order to determine if the $\delta^{34}S_{sulfide}$ trends are due to
477 progressive consumption of the sulfate reservoir (i.e., Rayleigh isotope fractionation or the
478 reservoir effect), we use an approximation of the isotopic evolution of the product of an
479 irreversible reaction in closed-system (after Mariotti et al., 1981):
480
481 $$\delta^{34}S_{H2S,d} = -\frac{\varepsilon(1-f)\ln(1-f)}{f} + \delta^{34}S_{SO4,0} \quad \text{(eqn. 4)}$$
482
483 Where $\delta^{34}S_{H2S,d}$ is the sulfur isotope composition of sulfide at depth d, ε is the average apparent
484 sulfur isotope fractionation effect ($^{34}\varepsilon_{MSR}$), f is the fraction of sulfate remaining at depth d, and
485 $\delta^{34}S_{SO4,0}$ is the sulfur isotope composition of sulfate when f = 0. This approximation linearizes
486 the relationship between the fraction of sulfate remaining and $\delta^{34}S_{H2S}$ value at each depth such
487 that the slope of the line is the average apparent sulfur isotope fractionation that is likely
488 dominated by sulfate reduction ($^{34}\varepsilon_{MSR}$) and the y-intercept is the S isotope composition of the
489 sulfate reservoir ($\delta^{34}S_{SO4,0}$; Mariotti et al., 1981; Mandernack et al., 2003). We used the
490 porewater $\delta^{34}S_{sulfide}$ data from the afternoon purple mat profile and sulfate concentration data
491 from cores sampled in the purple mat in the afternoon as inputs into the equation. These data fit a
492 linear regression (r^2 = 0.95, n = 12) where the slope of the line is -22.7‰ and the y-intercept is

18.8‰ (Figure 7). The value for $^{34}\varepsilon_{MSR}$ predicted from this model (-22.7‰) is within the range of sulfur isotope fractionations during sulfate reduction reported for microbial mats at Solar Lake (Habicht and Canfield, 1997), which had similar sulfate reduction rates to those measured here. Additionally, the $\delta^{34}S_{SO4,0}$ value (18.8‰) is similar (i.e., within uncertainty of 0.2‰) to the $\delta^{34}S$ value of sulfate emanating from the alcove (18.9‰). Setting the y-intercept to the $\delta^{34}S$ value of sulfate emanating from the alcove (18.9‰) yields a similar $^{34}\varepsilon_{MSR}$ value (-22.8‰) to that predicted by the porewater data alone (-22.7‰). Thus, the $\delta^{34}S_{sulfide}$ data can be explained by progressive consumption of the sulfate reservoir with depth such that deep $\delta^{34}S_{sulfide}$ values approach the $\delta^{34}S$ value of the sulfate reservoir.

Porewater sulfide sulfur isotope ($\delta^{34}S_{sulfide}$) patterns vary throughout the day in both purple and grey diffuse mats at Middle Island Sinkhole (MIS; Figure 5). Given that $\delta^{34}S_{sulfide}$ patterns are driven by progressive consumption of the sulfate reservoir, changes in the $\delta^{34}S_{sulfide}$ values throughout the day are caused by variation in net sulfate consumption with depth in the mat and underlying sediment. In particular, when the sulfate reservoir is nearly completely consumed, $\delta^{34}S_{sulfide}$ values approach the $\delta^{34}S$ value of the overlying sulfate reservoir. The depth where $\delta^{34}S_{sulfide}$ values reach ~15-18‰ moves between 1.5 and 7.5 cm throughout the day. While changes in geochemistry within and immediately adjacent to the ~2 mm-thick mat may be driven by light cycles, light only penetrates down to ~750 μm within the mat (Merz et al., 2020). Therefore, the deep (up to 7.5 cm below the SWI) $\delta^{34}S_{sulfide}$ dynamics are unlikely due directly to diurnal trends in light availability. Instead, we must ask what processes influence variation in rates of sulfate reduction and sulfide oxidation at different depths in the mat and sediment over diurnal cycles. In what follows, we review diurnal changes in the geomicrobiology of the surface mat and then explore potential mechanisms – migration of bacteria, migration of diatoms, sulfide oxidation by cable bacteria – that potentially drive $\delta^{34}S_{sulfide}$ trends in the sediment underlying the mat.

The purple mats contain cyanobacteria capable of both anoxygenic and oxygenic photosynthesis, large sulfide-oxidizing bacteria, and sulfate-reducing bacteria including some with the genetic potential for sulfur disproportionation (Nold et al., 2010a; Voorhies et al., 2012; 2016; Klatt et al., 2017; Sharrar et al., 2017; Grim, 2019; Biddanda and Weinke, accepted). Over a diurnal light cycle, activity in the purple mat transitions between predominantly anoxygenic

photosynthesis in the morning until the early afternoon to simultaneous anoxygenic and oxygenic photosynthesis in the afternoon and evening (Figure 8; Klatt et al., 2017; Biddanda and Weinke, accepted). These diurnal changes are linked with changes in the surface appearance of the mat; the surface of the mat is white in the morning because it is dominated by chemosynthetic sulfide-oxidizing bacteria, becomes purple in the afternoon when purple cyanobacteria are at the surface, and then becomes white again in the late evening and night (Klatt et al., 2017; Biddanda and Weinke, accepted). Anoxygenic photosynthesis throughout the day is sustained by the sulfide flux from underneath the mat and local sulfide production within the photic zone (Voorhies et al., 2012). This is consistent with the observation that the mat and sediment between 0 and 1 cm depth below the SWI have high rates of sulfate reduction relative to the sediment below (1803.7 nmol ± 896.8 nmol cm^{-3} d^{-1} at 0.5cm versus ~25 to ~835 nmol cm^{-3} d^{-1} in the deeper sediment; Figure 3; Table S1). The consumption of sulfate by sulfate reduction near the surface may also play a role in limiting diffusion of sulfate to the deeper sediment. The grey mat lacks cohesion at the surface and does not have the purple cyanobacteria that drive changes in rates of gross anoxygenic and oxygenic photosynthesis throughout the day. The grey mat does contain a diffuse layer of chemosynthetic sulfide-oxidizing bacteria that can play a role in sulfide oxidation at the mat surface (Klatt et al., 2017; Biddanda and Weinke, accepted). Although diurnal changes in geomicrobiological cycling in the surface mat impact net sulfate consumption and $\delta^{34}S_{sulfide}$ values near the SWI, additional processes that vary with depth throughout the day must drive the deeper (> 1 cm) $\delta^{34}S_{sulfide}$ trends.

Many bacterial taxa capable of motility have been identified in the MIS mats (Nold et al., 2010a; Voorhies et al., 2012; Biddanda et al., 2015). If motile bacteria in the mats are able to migrate to depths >1 cm below the SWI, their activities could play a role in diurnal changes in deep $\delta^{34}S_{sulfide}$ trends. For example, some migratory filamentous sulfide-oxidizing bacteria can reduce intracellular reservoirs of elemental sulfur to sulfide (Schwedt et al., 2012). A diurnal migration over this distance would imply a migration speed of >2 µm s^{-1}, which is in the range of previously reported values (e.g., Dunker et al., 2011). However, large vacuolated filamentous sulfur oxidizers similar to the sulfide-oxidizing bacteria with intracellular elemental reservoirs that have been the subject of the migratory studies have not been found at MIS (Nold et al., 2010a; Kinsman-Costello et al., 2017; Merz et al., 2020). Thus, although the large sulfide-oxidizing bacteria at MIS may migrate down and release elemental sulfur or sulfide at depth, it is

554 unlikely that the sulfide-oxidizing mat-forming microbial communities alone shape these
555 patterns. Another option is that the zone of sulfate reduction moves due to migration of sulfate-
556 reducing bacteria. Sulfate-reducing bacteria have been reported to reach a speed of up to 63 µm
557 s^{-1} in aqueous solution (Krekeler et al., 1998). As migration over multiple cm has not been
558 observed previously, this would represent an extreme rate of migration of these taxa on a daily
559 basis, with unknown competitive advantage considering the energetic requirements for
560 migration. Thus, it is unlikely that migration of either sulfide-oxidizing or sulfate-reducing
561 bacteria drives the deep $\delta^{34}S_{sulfide}$ trends.
562 Diatoms are common components of benthic microbial mat ecosystems (Longphuirtet al.,
563 2009; Guarini et al., 2008; Cahoon, 1991; Macintyre et al., 1996) and have been shown to
564 migrate vertically over diurnal cycles (Cartaxana et al., 2008; Pinckley and Zingmark, 1991;
565 Round and Palmer, 1966). Diatoms also are one of the few eukaryotic taxa that are capable of
566 dissimilatory nitrate reduction to ammonium (DNRA) using intracellularly stored nitrate (Kamp
567 et al., 2011). In the MIS mats and sediment, the migration of diatoms is linked to variations in
568 rates of DNRA (Merz et al., 2020). Isotope labeling indicates that these migrating diatoms take
569 up nitrate near the SWI in the afternoon and then migrate downward where they conduct DNRA.
570 The diatoms reach maximum depths of 4 cm between ~2am and 7am, before returning to the
571 SWI at around noon (Figure 8). This diurnal migration matches diurnal variations in the depth
572 where sulfate is nearly completely consumed (as indicated by the depth where $\delta^{34}S_{sulfide}$ values
573 approach $\delta^{34}S$ values of the sulfate reservoir) in the grey mats. Thus, it is possible that oxidants
574 transported by the vertical migration of diatoms directly or indirectly stimulate sulfide oxidation
575 at cm-scale depths in the sediment below the grey mats. While the depth where sulfate is nearly
576 completely consumed below the purple mats is similar to maximum depths that diatoms reach in
577 the morning, evening, and night, either these taxa migrate to greater depths in the afternoon than
578 have been shown previously or additional processes are necessary to explain the sulfur isotope
579 geochemistry of the purple mats in the afternoon.
580 Cable bacteria are filamentous microorganisms that oxidize hydrogen sulfide by
581 transporting electrons along cm-scale distances in sediment (Nielsen et al., 2010; Pfeffer et al.,
582 2012). Although these sulfide-oxidizers are appealing candidates for explaining the deep (>1 cm)
583 $\delta^{34}S_{sulfide}$ trends, none of the 16S rRNA gene data from 0-12 cm depths matches with >95%
584 similarity to known cable bacteria 16S rRNA genes (Grim, 2019), indicating that there are no

taxa at MIS that are similar at the genus level to known cable bacteria (Kjeldsen et al., 2019). It is possible that taxonomically novel cable bacteria are present at MIS. However, pH profiles (Figure 4) do not display the pH typology associated with sulfide oxidation via cable bacteria and changes in O_2 concentration in the surface layer and water column did not change sulfide concentrations with depth over ~30 min to 1 hour timescales (Nielsen et al., 2010; Pfeffer et al., 2012; Seitaj et al., 2015). The apparent absence of cable bacteria might be due to sediment reworking by diatoms inhibiting their activity (Malkin et al., 2014). Thus, although we cannot rule out that cable bacteria are impacting diurnal $\delta^{34}S_{sulfide}$ trends, we currently lack evidence that these taxa are present at MIS.

We still lack an explanation for why the depth where sulfate is completely consumed increases to 7.5 cm in the afternoon in the sediment underlying the purple mat. The shape of the $\delta^{34}S_{sulfide}$ profile in the afternoon in the purple mat sediment is similar to the night and morning profiles, but shifted 1-2 cm lower. Net oxygen production in the purple mat may result in higher rates of sulfide oxidation near the SWI and play a role in shifting the $\delta^{34}S_{sulfide}$ profile lower. This is consistent with poor sulfide recovery in samples closest to the SWI. Thus, the activity of phototrophic organisms in the surface mat may influence the differences in the depth at which sulfate is nearly completely consumed between the purple and gray mats by impacting other organisms. The migration patterns of the diatoms are shaped by the amount of nitrate captured near the surface and the rate at which they consume it at depth (Merz et al., 2020). Therefore, it is possible that oxidant production by cyanobacteria in the purple mat promotes nitrification and increases the amount of nitrate that diatoms can store, enabling the diatoms to travel to greater depths in the purple mat than in the grey mat. In sum, although it is likely that the diurnal $\delta^{34}S_{sulfide}$ patterns are determined by the activity of both the surface mat communities and migrating diatoms (Figure 8), we cannot rule out that other geomicrobiological processes (e.g., motile bacteria or cable bacteria) are also impacting the sulfur cycle over cm-scales in the sediment underlying the mat.

4.2 Comparison with other modern microbial mats

Previous work on diurnal trends in sulfur isotope geochemistry of microbial mats was done with mats from Guerrero Negro, Baja California Sur, Mexico (Fike et al., 2009). Guerrero Negro

mat $\delta^{34}S_{sulfide}$ patterns were documented at higher spatial resolution (i.e., sub-mm resolution over ~1 cm length scale) than our results from MIS (i.e., cm resolution over ~8-20 cm). Nonetheless, both systems show changes in $\delta^{34}S_{sulfide}$ values over diurnal cycles. Sulfide in Guerrero Negro mats is ^{34}S-enriched by ~20-25‰ in the top 1-2mm of the mat relative to the deep portions (Fike et al., 2008; 2009) and there was vertical migration of the $\delta^{34}S_{sulfide}$ pattern over diurnal cycles (Fike et al., 2009). The $\delta^{34}S_{sulfide}$ trends were attributed to differential metabolic activity of S cycling microorganisms throughout the mats; higher rates of sulfate reduction and/or sulfide oxidation at the mat surface result in lower sulfur isotope fractionations between sulfate and sulfide such that $\delta^{34}S_{sulfide}$ values are higher at the surface. Greater light intensity at Guerrero Negro relative to MIS impacts oxidant availability (Canfield and Des Marais, 1993), which may promote sulfide oxidation at Guerrero Negro and thus the differential metabolic effect over the reservoir effect in determining $\delta^{34}S_{sulfide}$ patterns at Guerrero Negro. The striking difference between MIS and Guerrero Negro $\delta^{34}S_{sulfide}$ patterns could be due to the different resolution of measurements, with the cm-resolution here masking a potential enrichment at the surface. However, the microbial mats from Little Ambergris Cay, Turks and Caicos Islands show a similar pattern as Guerrero Negro of ^{34}S-depleted sulfide near the mat surface over cm-scales (Gomes et al., 2020). Although only measured during the daytime, this $\delta^{34}S_{sulfide}$ pattern was attributed to differential metabolic activity, with a potential additional influence of mixing of sulfide with different $\delta^{34}S_{sulfide}$ signatures due to tidal pumping. No ^{34}S-enrichment in sulfide over cm-scales was documented in a study of sulfur isotope geochemistry in cyanobacterial mats at Solar Lake, Sanai, Egypt, however no peak in sulfate-reduction rates was documented in situ (Habicht and Canfield, 1997). Thus, sulfur isotope geochemistry at MIS is different than these previously studied mat sites because the $\delta^{34}S_{sulfide}$ pattern over cm-scales is dominated by progressive consumption of the sulfate reservoir rather than differential metabolic activity, despite sulfate reduction rates being highest at the surface (Figure 5).

A potential explanation for the difference in the shape of $\delta^{34}S_{sulfide}$ profiles between MIS and previously studied mat sites is the difference in sulfate concentration between these systems. The previously studied sites have salinities greater than seawater and therefore sulfate concentrations greater than seawater concentrations (28mM; Fike et al., 2008; 2009; Habicht and Canfield, 1997; Gomes et al., 2020). Importantly, sulfide production was not sufficient to

646 completely consume the sulfate reservoir at any of these sites (Fike et al., 2008; 2009; Habicht
647 and Canfield, 1997; Present et al., 2018). In contrast, sulfate concentrations in water overlying
648 the mat at MIS are ~7.1 ± 1.5 mM (Kinsman-Costello et al., 2017), with some of the variation in
649 sulfate concentration due to hydrologically driven differences in mixing between alcove water
650 and Lake Huron water. Given the relatively low sulfate concentrations at MIS and high
651 availability of organic matter (Nold et al. 2013, Kinsman-Costello et al., 2017, Rico and
652 Sheldon, 2019), sulfate is almost completely exhausted at depths of ~1-8cm (Figure 3; Kinsman-
653 Costello et al., 2017) such that $\delta^{34}S$ values of deep sulfide are similar to those of the overlying
654 sulfate (Figure 5). Thus, sulfate concentrations at MIS are sufficiently low that progressive
655 consumption of the sulfate reservoir dominates over differential metabolic activity in
656 determining $\delta^{34}S_{sulfide}$ patterns over cm-scales.
657 Another important factor promoting consumption of the sulfate reservoir at MIS is organic
658 matter. MIS hosts a thin (~2 mm) microbial mat overlying lake sediments. The sedimentary
659 organic matter underlying the MIS mats has geochemical characteristics more similar to settling
660 phytoplankton than the microbial mat biomass (Nold et al., 2013; Rico and Sheldon, 2019). Deep
661 anaerobic communities are thus able to utilize labile planktonic biomass rather than microbial
662 mat biomass, which can contain abundant cyanobacterial sheaths that are relatively resistant to
663 microbial decay (Horodsyki et al., 1992; Bartley, 1996). This enables sulfate reduction to
664 exhaust the sulfate reservoir at depth, as is common in organic-rich marine sediments composed
665 of labile planktonic biomass (e.g., Aller et al., 1996). In contrast, in the Guerrero Negro mats,
666 high rates of organic matter remineralization at the surface consumes labile organic matter
667 (Canfield and Des Marais, 1993), leaving mat material below composed primarily of degraded
668 organic matter (Lee et al., 2019). Similarly, the organic matter below the ~1cm-thick pigment-
669 rich layer at the surface of the Little Ambergris Cay mats is composed of diagenetically-altered,
670 chemically-recalcitrant organic matter (Gomes et al., 2020). The presence of degraded organic
671 matter at depth may limit sulfate reduction, proving insufficient to fully consume the sulfate
672 reservoir at depth in these other mat sites. Incomplete sulfate reduction may also be a result of
673 microbial communities with sulfate transporters adapted to the high sulfate concentrations (> 40
674 mM) of these systems (Bradley et al., 2016). In sum, differences in $\delta^{34}S_{sulfide}$ trends between MIS
675 and previously studied mat sites can be attributed to sulfate reduction being limited by electron
676 acceptors versus electron donors, respectively.

677

678 4.3 Solid-phase sulfide $\delta^{34}S_{sulfide}$ signatures

679

680 Pyrite is a major geological archive of sulfide and thus $\delta^{34}S$ values of pyrite and other
681 sulfide minerals have been used to evaluate patterns of sulfur cycling and environmental
682 conditions in ancient sediments and microbial mats (see review in Fike et al., 2015). Here, we
683 compare $\delta^{34}S_{sulfide}$ patterns to $\delta^{34}S$ values in two solid-phase sulfide pools: (1) acid-volatile
684 sulfides (AVS), which are primarily composed of iron monosulfides that are an important
685 intermediates in some pyrite formation pathways (Rickard and Luther, 2007; Rickard, 2012), and
686 (2) chromium-reducible sulfides (CRS), which are primarily composed of pyrite and elemental
687 sulfur (Canfield et al., 1986), with the latter potentially playing a role in the polysulfide pathway
688 when elemental sulfur reacts with sulfide to form polysulfides (Rickard and Luther, 2007;
689 Rickard, 2012). Trends in $\delta^{34}S$ values differ between AVS, CRS, and porewater sulfide (Figure
690 6). AVS $\delta^{34}S$ values are more variable (range from -7.3 to 18.5‰, σ = 8.1‰, n = 11) than CRS
691 $\delta^{34}S$ values (range from -10.4 to 0.9‰, σ = 3.9‰, n = 14). Trends in $\delta^{34}S_{AVS}$ values with depth
692 are somewhat similar to $\delta^{34}S_{sulfide}$ trends; $\delta^{34}S_{AVS}$ values are low below the SWI and increase
693 with depth. However, only one measured $\delta^{34}S_{AVS}$ value was within the range of high $\delta^{34}S_{sulfide}$
694 values (~15 to 18‰) measured in the deep porewater (below 1.5 to 7.5 cm, depending on the
695 time of day and mat type). Other $\delta^{34}S_{AVS}$ values measured below 2.5 cm ranged from -0.1 to
696 9.9‰. There is a subtle increase in $\delta^{34}S_{CRS}$ values with depth, but $\delta^{34}S_{CRS}$ values remained
697 between -10.4 and 0.9‰.

698 In order to improve interpretations of $\delta^{34}S_{CRS}$ values preserved in ancient low-oxygen
699 microbial mat environments, it is useful to explore how $\delta^{34}S_{CRS}$ values relate to porewater
700 $\delta^{34}S_{sulfide}$ values. Porewater $\delta^{34}S_{sulfide}$ values vary over diurnal cycles and vary between mat types.
701 In contrast, sedimentary $\delta^{34}S_{CRS}$ values represent a time-averaged signal because sediment
702 accumulates at a rate of ~0.3 g cm^{-2} $year^{-1}$ (Nold et al., 2013). It is also necessary to consider the
703 timescale of change of mats at the SWI. The appearance of the mat (e.g., purple versus grey or
704 white patches) varies over seasonal and annual timescales (Grim, 2019; cf., Nold et al., 2010a;
705 Voorhies et al., 2012; 2016; Kinsman-Costello et al., 2017). Thus, the sediment integrates $\delta^{34}S$
706 signatures such that $\delta^{34}S_{CRS}$ values represent an average of the geochemical conditions of

sediment covered by different mat types, similar to other sedimentary environments (e.g., Houghton et al., 2019).

Spatial variability in solid phase sulfide formation (i.e., AVS or CRS) can also impact $\delta^{34}S_{CRS}$ and $\delta^{34}S_{AVS}$ signatures. Previous work showed that there is not significant formation of pyrite in the sediment underlying the microbial mat. In particular, Rico and Sheldon (2019) reported iron speciation data from 9 cores sampled in October 2014 and June 2016 which showed no increase in pyrite concentrations with depth in the sediment (Figure 6). These results are consistent with our observation that $\delta^{34}S_{CRS}$ values are similar to $\delta^{34}S_{sulfide}$ values proximal to the microbial mat and indicate that $\delta^{34}S_{CRS}$ values are primarily capturing $\delta^{34}S_{sulfide}$ signatures near the SWI. There is a slight ^{34}S-enrichment (at most ~10‰) in CRS with depth, which could be due to the minor additional CRS formation (i.e., pyrite or elemental sulfur) deeper in the sediment and inheritance of δ^{34}S signatures of the corresponding sulfide, AVS, or polysulfides. Elemental sulfur produced from chemotrophic oxidation of sulfide is slightly ^{34}S-enriched relative to the sulfide (e.g., Zerkle et al., 2016). Thus, the ^{34}S-enrichment in CRS with depth could be due to the incorporation of ^{34}S-enriched elemental sulfur into the CRS pool and/or formation of pyrite via the polysulfide pathway with the ^{34}S-enriched elemental sulfur serving as a polysulfide precursor. However, given that there is no increase in pyrite concentrations with depth, it is unlikely that the amount of additional pyrite formed over the studied depth interval (0 to ~20cm) is greater than the relative uncertainty associated with the pyrite concentration analysis (replicate analyses have a relative standard deviation of ~ 12%; Rico and Sheldon, 2019). Further, decreases in AVS concentrations with depth in sediment have been shown to be due to dissolution of metastable iron monosulfide precipitates to aqueous iron monosulfides, rather than transformation of AVS to CRS (Rickard et al., 1999). Thus, although we cannot rule out that some AVS dissolves and then precipitates as pyrite in the deeper (>1 cm) sediment, we lack evidence for substantial pyrite formation at depth (Figure 6; Rico and Sheldon, 2019). Thus, the CRS pool, which is likely to be the most geologically stable sulfide pool, is primarily formed near the microbial mat at the SWI and captures δ^{34}S signatures sulfide in that location.

Sulfur cycling within the mat may play a role in promoting pyrite formation near the SWI. Both sulfate-reducing and sulfide-oxidizing taxa have been documented in the surface mat (Nold et al., 2010a) and sediments (0-3cm; Kinsman-Costello et al., 2017). Various types of sulfide-oxidation processes produce S^0 or other sulfur intermediates near the mat surface. In

particular, anoxygenic photosynthetic cyanobacteria at MIS produce these sulfur intermediates and immediately secrete them to their surroundings (Nold et al., 2010a). These intermediate sulfur species can react with sulfide to form polysulfides, which promote CRS formation via the polysulfide pathway (eqn. 2; Rickard, 1975, Rickard and Luther, 2007). Besides producing intermediate sulfur species, experimental studies have shown that other activities of microorganisms can promote pyrite formation. The formation of iron sulfide precursors to pyrite can occur on cell surfaces of sulfate-reducing microorganisms (Picard et al., 2018). Pyrite formation can also be coupled to methane production in microbial cultures containing sulfate-reducing bacteria and methanogens (Thiel et al., 2019). In Santa Barbara Basin, it was proposed that pyrite formed in biofilms rather than in sedimentary pore waters (Raven et al., 2016). Thus, although iron geochemistry may have played a role in limiting the depth interval over which pyrite formation could occur (Rico and Sheldon, 2019), it is likely that the production of sulfur intermediates that could react with sulfide to form polysulfide and other microbial activity also played a role in promoting pyrite formation near the SWI.

These results have implications for studies of both bulk and high-spatial resolution sedimentary sulfur isotope geochemistry of sediments interpreted to be formed in microbial mat environments (e.g., Wacey et al., 2010; Fischer et al., 2014; Meyer et al., 2017; Gomes et al., 2018). Specifically, our results and iron speciation data (Rico and Sheldon, 2019) indicate that pyrite formation primarily occurs near the surface microbial mat (within the top 1 cm), where microbial activity can promote pyrite formation. Therefore, in systems like MIS, $\delta^{34}S_{CRS}$ values preserve information about environmental conditions at the mat surface and are only minimally influenced by early diagenetic processes that affect deeper portions of the sediment. This is in part due to iron geochemistry that is unfavorable to further CRS precipitation in deeper portions of the mat, as indicated by invariant pyrite concentrations (Figure 6) and iron speciation with depth in the sediment (Rico and Sheldon, 2019). In ancient oceans with more abundant iron, it is possible that iron geochemistry more favorable to CRS formation could have extended the zone of CRS formation deeper into the sediment, resulting in the incorporation of deeper sulfide and/or AVS into early diagenetic pyrite. Of course, later diagenetic processes can also affect $\delta^{34}S_{CRS}$ values and therefore petrography or additional chemical tools should be used to assess evidence for further post-depositional sulfide formation or transformation. Petrographically constrained micro-scale $\delta^{34}S_{pyrite}$ analyses can be used to infer different phases of sulfide

formation, as well as other phases of post-depositional metal sulfide formation and/or recrystallization, especially when done in conjunction with other high-spatial resolution geochemical analyses (e.g., Wacey et al., 2010; Meyer et al., 2017; Fischer et al., 2014; Gomes et al., 2018; Cui et al., 2018; Bryant et al., 2019). These studies can be used to discern if sulfur cycling within ancient mat environments was more similar to those documented in higher sulfate (>28 mM) environments dominated by recalcitrant cyanobacterial biomass (Fike et al., 2008; 2009; Lee et al. 2019; Gomes et al., 2020) or in mats like MIS characterized by planktonic-sourced organic matter and substantial consumption of the ambient sulfate reservoir.

In the low-oxygen system at MIS, low sulfate concentrations (~7.1 ± 1.5mM; Kinsman-Costello et al., 2017) result in sulfur isotope geochemistry dominated by progressive consumption of the sulfate reservoir rather than differential metabolic activity. The diurnal $\delta^{34}S_{sulfide}$ variability is shaped by both geomicrobiological cycling in the surface mat and the activities of migrating diatoms. This style of geomicrobiological cycling is not known to be common in the modern ocean and it is unclear if it was common in the past. Therefore, it is not our intention to imply that similar migratory activity shaped $\delta^{34}S_{sulfide}$ trends in ancient oceans dominated by microbial mat ecosystems. Whatever taxa were present in ancient microbial mat ecosystems, electron-donor versus electron-acceptor limitation would have impacted $\delta^{34}S_{sulfide}$ trends (i.e., if they are driven by differential metabolic activity versus progressive consumption of the sulfate reservoir) and iron geochemistry would have impacted the location of pyrite formation. At MIS, low sulfate concentrations (~7.1 ± 1.5 mM), labile planktonic biomass, and iron geochemistry all result in early diagenetic pyrite that captures $\delta^{34}S$ signatures of pore water sulfide near the SWI of the low-oxygen microbial mat.

5. Conclusions

Geomicrobiological cycling in low-oxygen microbial mats at Middle Island Sinkhole results in dynamic $\delta^{34}S_{sulfide}$ patterns over diurnal cycles that span depths well below the microbial mats. The diurnal cycles primarily affect $\delta^{34}S_{sulfide}$ values near the sediment-water interface, where $\delta^{34}S_{sulfide}$ values range from -7.1 to 11.1‰. The availability of oxidants and transport of oxidants by migrating taxa have cascading effects on net sulfate-reduction rates deeper in the sediment. The consumption of the sulfate reservoir in deeper sediments results in $\delta^{34}S_{sulfide}$ trends where

sulfide is ^{34}S-depleted at the surface and becomes ^{34}S-enriched with depth, approaching $\delta^{34}S$ values of the overlying sulfate reservoir. Despite the dynamic diurnal $\delta^{34}S_{sulfide}$ patterns, pyrite captures $\delta^{34}S$ signatures of the ambient sulfide at the locus of its formation at or immediately adjacent to the surface microbial mat. Thus, the chromium-reducible sulfur pool, usually considered to be composed primarily of pyrite, captures $\delta^{34}S$ signatures near the sediment-water interface and is only minimally altered by deeper early diagenetic processes. In addition to the role of the low-oxygen microbial mat communities, these $\delta^{34}S$ patterns are also likely due to a relatively low sulfate concentrations (~7 mM), inputs of labile planktonic biomass, and limited iron availability. These results, and their contrast with those from other mat systems in distinct geochemical and environmental settings such as Guerrero Negro, have implications for the interpretations of both bulk and fine-scale studies of $\delta^{34}S$ signatures of pyrite in sediments formed in microbial mat environments. Specifically, bulk $\delta^{34}S$ values will integrate $\delta^{34}S_{sulfide}$ signals over the location of pyrite formation, which is primarily the mat surface at MIS. Microanalytical studies of $\delta^{34}S$ values of pyrite may document individual pyrite grains with $\delta^{34}S$ values that span the range of $\delta^{34}S_{sulfide}$ values at the mat surface with a mean $\delta^{34}S$ value corresponding to the bulk pyrite $\delta^{34}S$ value.

Data Availability Statement

The data that supports the findings of this study are available in the supplementary material of this article.

Acknowledgements

We thank the NOAA Thunder Bay National Marine Sanctuary Dive Unit – John Bright, Russ Green, Phil Hartmeyer, Wayne Lusardi, Stephanie Gandulla, Katie Clevenger, and Annie Wright – and R/V Storm Ship Captain Travis Smith for field support, site access, and sampling. We also thank Dirk de Beer, Arjun Chennu, Bopaiah Biddanda, Dack Stuart, Greg Druschel, Martin Kurek, Chase Howard, John Shukle, Hui Chien Tan, and Heidi Babos for help with field science operations and useful conversation and Stephanie Moore for laboratory and technical assistance. This work was supported by NSF grant EAR-1637066 to G.J.D. and W.Z.

Figure and table captions:

Figure 1 Bathymetric image of Middle Island Sinkhole (from Nold et al., 2013) with sampling grid in white and showing locations of purple mat photo film deployments (purple box), grey mat photo film deployments (orange box), core for solid phase sulfide (SPS) sediment geochemistry (black box), cores for sulfate reduction rate (SRR) and porewater sulfate concentration ($[SO_4^{2-}]$) determination (yellow box), and cores for ex situ microsensor measurements (red box).

Figure 2 Black and white photo film deployed in (A) a purple mat location and (B) a grey mat location in the afternoon (15:00 – 17:30). Film width is 25.4cm. Deployment times of all films are provided in Table 1.

Figure 3 Porewater sulfate concentration ($[SO_4^{2-}]$; left) and sulfate reduction rates (SRR; right) from dark incubations. Grey symbols show the results of individual analyses with analytical errors smaller than the size of the symbol. The solid black line is the average of all analyses. Data are provided in Table S1.

Figure 4 Profiles of pH (black circles), O_2 concentrations (blue squares), and total sulfide concentrations ($\Sigma[S^{2-}]$, $[HS^-]$, $[H_2S]$, where brackets denote concentration; red triangles) from ex situ microsensor measurements under light (58 µmol photons m^{-2} s^{-1}; open symbols) and dark, low O_2 (<0.5 µmol photons m^{-2} s^{-1} and ~13 µM O_2; closed symbols) conditions measured within ~1 hour in the same location in a core with a surface purple mat. Data are provided in Table S2.

Figure 5 Porewater sulfide sulfur isotope ($\delta^{34}S_{sulfide}$) values from purple (left) and diffuse grey (right) mat locations. The sulfur isotope composition of sulfate ($\delta^{34}S_{sulfate}$) in water emerging from the alcove is indicated on both plots with a dashed line. Reproducibility of S isotope measurements is 0.2‰ (i.e., within the size of the symbols) based on standard deviation of international standard analyses. Deployment times are provided in Table 1. Data are provided in Table S3.

Figure 6 Solid phase sulfur and iron geochemistry. Left: Sulfur isotope composition ($\delta^{34}S$) of acid volatile sulfide (AVS; squares) and chromium reducible sulfide (CRS; diamonds) from cores taken in July 2015 (grey) and October 2015 (black). The range of $\delta^{34}S_{sulfide}$ values in porewater from the purple and grey diffuse mat locations are shown in shaded purple and orange, respectively. Reproducibility of S isotope measurements is 0.2‰ (i.e., within the size of the symbols) based on standard deviation of international standard analyses. Data are provided in Table S4. Right: Concentration of Fe as pyrite (wt %) from nine cores taken in 2014 and 2015 from data published in Rico and Sheldon (2019).

Figure 7 Porewater sulfide sulfur isotope evolution using the Mariotti et al. (1981) approximation of isotopic evolution of a product of a reaction with a kinetic isotope effect in a closed system. The linear regression predicts the average apparent sulfur isotope fractionation effect that is most likely dominated by microbial sulfate reduction ($^{34}\varepsilon_{MSR}$) as the slope of the line and the sulfur isotope composition of the initial sulfate reservoir as the y-intercept.

Figure 8 Schematic showing diurnal changes in the depth of near complete sulfate consumption in sediment underlying purple (top) and grey (bottom) mats. Purple and white lines near the sediment water interface indicate filamentous purple cyanobacteria and sulfide-oxidizing bacteria, respectively. Green ovals depict migratory diatoms.

Table 1 Deployment times and durations for photo films used to trap porewater sulfide over a diurnal cycle to determine pore water $\delta^{34}S_{sulfide}$ patterns.

Supplementary Files:

Supplementary document with figures showing pictures of: the back of photo films deployed to trap sulfide for determination of sulfur isotope ($\delta^{34}S$) values of porewater sulfide; the front of photo films deployed to trap sulfide for determination of $\delta^{34}S$ values of porewater sulfide; and pictures of films deployed in the field.

Table S1: Sulfate concentration and sulfate reduction rates (SRR) from dark incubations of cores obtained on July 27, 2016 and July 28, 2016 (data shown in Figure 3).

Table S2: Ex situ microsensor pH, O_2 concentration, and total sulfide concentration values for light (58 µmol photons m^{-2} s^{-1}) and dark (<0.5 µmol photons m^{-2} s^{-1} and ~13 µM O_2 in the overlying water column) conditions (data shown in Figure 4).

Table S3: Sulfur isotope composition of porewater sulfide over a diurnal cycle. Sulfide yields in units of µmoles S/cm^2 of film are also provided. (data shown in Figure 5).

Table S4: Sulfur isotope composition and concentration of acid-volatile sulfide and chromium-reducible sulfide (data shown in Figure 6).

References

Aller, R. C., Blair, N. E., Q. Xia, Q., and Rude, P. D., 1996, Remineralization rates, recycling, and storage of carbon in Amazon shelf sediments: Continental Shelf Research, v. 16, p. 753-786.

Balci, N., Shanks, I., W. C., Mayer, B., and Mandernack, K. W., 2007, Oxygen and sulfur isotope systematics of sulfate produced by bacterial and abiotic oxidation of pyrite: Geochimica et Cosmochimica Acta, v. 71, p. 3796–3811.

Bao, H., 2006, Purifying Barite for Oxygen Isotope Measurement by Dissolution and Reprecipitation in a Chelating Solution: Anal. Chem., v. 78, p. 304-309.

Bartley, J. K., 1996, Actualistic taphonomy of cyanobacteria: Implications for the Precambrian fossil record: Palaios, v. 11, p. 571–586.

Biddanda, B. A., Coleman, D. F., Johengen, T. H., Ruberg, S. A., Meadows, G. A., Van Sumeren, H. W., Rediske, R. R., and Kendall, S. T., 2006, Exploration of a submerged sinkhole ecosystem in Lake Huron: Ecosystems, v. 9, p. 828–842.

Biddanda, B. A., McMillan, A. C., Long, S. A., Snider, M. J., and Weinke, A. D., 2015, Seeking sunlight: Rapid phototactic motility of filamentous mat- forming cyanobacteria optimize photosynthesis and enhance carbon burial in Lake Huron's submerged sinkholes: Front. Microbiol., v. 6, p. 1–13.

Biddanda, B. A., and Weinke, A. D., accepted, Extant mat world analog microbes synchronize migration to a diel tempo: Limnology and Oceanography, https://doi.org/10.1002/essoar.10502762.10502761.

Bottcher, M. E., Thamdrup, B., and Vennemann, T. W., 2001, Oxygen and sulfur isotope fractionation during anaerobic bacterial disproportionation of elemental sulfur: Geochimica et Cosmochimica Acta, v. 65, p. 1601–1609.

Bradley, A. S., Leavitt, W. D., Schmidt, M., Knoll, A. H., Girguis, P. R., and Johnston, D. T., 2016, Patterns of sulfur isotope fractionation during microbial sulfate reduction: Geobiology, v. 14, no. 1, p. 91-101.

Bryant, R. N., Jones, C., Raven, M. R., Gomes, M. L., Berelson, W. M., Bradley, A. S., and Fike, D. A., 2019, Sulfur isotope analysis of microcrystalline iron sulfides using secondary ion mass spectrometry imaging: Extracting local paleo-environmental information from modern and ancient sediments: Rapid Communications in Mass Spectrometry, v. 33, p. 491-502.

Cahoon, L., 1999, The role of benthic microalgae in neritic ecosystems: Oceanography and marine biology, v. 37, p. 47-86.

Canfield, D. E., and Des Marais, D. J., 1993, Biogeochemical cycles of carbon, sulfur, and free oxygen in a microbial mat: Geochimica et Cosmochimica Acta, v. 57, p. 3971–3984.

950 Canfield, D. E., and Farquhar, J., 2009, Animal evolution, bioturbation, and the sulfate
951 concentration of the oceans: Proceedings of the National Academy of Science, v. 106, p. 8123-
952 8127.
953
954 Canfield, D. E., Raiswell, R. R., Westrich, J. T., Reaves, C. M., and Berner, R. A., 1986, The use
955 of chromium reduction in the analysis of reduced inorganic sulfur in sediments and shales:
956 Chemical Geology, v. 54, p. 149-155.
957
958 Cartaxana, P., Brotas, V., and Serôdio, J., 2008, Effects of two motility inhibitors on the
959 photosynthetic activity of the diatoms cylindrotheca closterium and pleurosigma angulatum:
960 Diatom Research, v. 23, p. 65-74.
961
962 Chanton, J. P., and Martens, C. S., 1985, The Effects of Heat and Stannous Chloride Addition on
963 the Active Distillation of Acid Volatile Sulfide from Pyrite-Rich Marine Sediment Samples:
964 Biogeochemistry, v. 1, no. 4, p. 375-382.
965
966 Cui, H., Kitajima, K., Spicuzza, M. J., Fournelle, J. H., Denny, A., Ishida, A., Zhang, F., and
967 Valley, J. W., 2018, Questioning the biogenicity of Neoproterozoic superheavy pyrite by SIMS:
968 American Mineralogist, v. 103, p. 1362-1400.
969
970 de Beer, D., Glud, A., Epping, E., and Kiihl, M., 1997, A fast-responding CO2 microelectrode
971 for profiling sediments, microbial mats, and biofilms: Limnology and Oceanography, v. 42, p.
972 1590-1600.
973
974 Des Marais, D. J., 2003, Biogeochemistry of hypersaline microbial mats illustrates the dynamics
975 of modern microbial ecosystems and the early evolution of the biosphere.: Biology Bulletin, v.
976 204, p. 160-167.
977
978 Dick, G. J., Grim, S. L., and Klatt, J. M., 2018, Controls on O2 Production in Cyanobacterial
979 Mats and Implications for Earth's Oxygenation: Annu. Rev. Earth Planet. Sci., v. 46, p. 123-147.
980

Donald, R., and Southam, G., 1999, Low temperature anaerobic bacterial diagenesis of ferrous monosulfide to pyrite: Geochimica et Cosmochimica Acta, v. 63, p. 2019-2023.

Dunker, R., Roy, H., Kamp, A., and Jorgensen, B. B., 2011, Motility patterns of filamentous sulfur bacteria, Beggiatoa spp: FEMS Microbiol Ecol, v. 77, no. 1, p. 176-185.

Fike, D. A., Bradley, A. S., and Rose, C. V., 2015, Rethinking the Ancient Sulfur Cycle: Annual Review of Earth and Planetary Sciences, v. 43, no. 1, p. 593-622.

Fike, D. A., Finke, N., Zha, J., Blake, G., Hoehler, T. M., and Orphan, V. J., 2009, The effect of sulfate concentration on (sub)millimeter-scale sulfide δ34S in hypersaline cyanobacterial mats over the diurnal cycle: Geochimica et Cosmochimica Acta v. 73, p. 6187–6204.

Fike, D. A., Gammon, C. L., Ziebis, W., and Orphan, V. J., 2008, Micron-scale mapping of sulfur cycling across the oxycline of a cyanobacterial mat: a paired nanoSIMS and CARD-FISH approach: ISME J, v. 2, no. 7, p. 749-759.

Fike, D. A., Houghton, J. L., Moore, S. E., Gilhooly, W. P., Dawson, K. S., Druschel, G. K., Amend, J. P., and Orphan, V. J., 2017, Spatially resolved capture of hydrogen sulfide from the water column and sedimentary pore waters for abundance and stable isotopic analysis: Marine Chemistry, v. 197, p. 26-37.

Fischer, W. W., Fike, D. A., Johnson, J. E., Raub, T. D., Guan, Y., and Kirschvink, J. L., 2014, SQUID–SIMS is a useful approach to uncover primary signals in the Archean sulfur cycle: Proceedings of the National Academy of Science, v. 111, p. 5468–5473.

Fossing, H., and Jørgensen, B. B., 1989, Measurements of bacterial sulphate reduction in sediments: evaluation of a single-step chromium reduction method: Biogeochemistry, v. 8, p. 205–222.

Gomes, M., Reidman, L. A., O'Reilly, S. S., Lingappa, U., Metcalfe, K., Fike, D. A., Grotzinger, J. P., Fischer, W. W., and Knoll, A. H., 2020, Microbial Mats on Little Ambergris Cay, Turks and Caicos Islands: Taphonomy and the Selective Preservation of Biosignatures: Frontiers in Earth Sciences, v. 8, p. 387.

Gomes, M. L., Fike, D. A., Bergmann, K. D., C. Jones, C., and Knoll, A. H., 2018, Environmental insights from high-resolution (SIMS) sulfur isotope analyses of sulfides in Proterozoic microbialites with diverse mat textures: Geobiology, v. 16, p. 17-34.

Gomes, M. L., and Hurtgen, M. T., 2013, Sulfur isotope systematics of a euxinic, low-sulfate lake: Evaluating the importance of the reservoir effect in modern and ancient oceans: Geology, v. 41, no. 6, p. 663-666.

Gomes, M. L., and Hurtgen, M. T., 2015, Sulfur isotope fractionation in modern euxinic systems: Implications for paleoenvironmental reconstructions of paired sulfate–sulfide isotope records: Geochimica et Cosmochimica Acta, v. 157, p. 39-55.

Gomes, M. L., and Johnston, D. T., 2017, Oxygen and sulfur isotopes in sulfate in modern euxinic systems with implications for evaluating the extent of euxinia in ancient oceans: Geochimica et Cosmochimica Acta, v. 205, p. 331-359.

Grim, S. L., 2019, Genomic and Functional Investigations Into Seasonally-Impacted and Morphologically-Distinct Anoxygenic Photosynthetic Cyanobacterial Mats [PhD: University of Michigan.

Grotzinger, J. P., and Knoll, A. H., 1999, Stromatolites in Precambrian Carbonates: Evolutionary Mileposts or Environmental Dipsticks?: Annu. Rev. Earth Planet. Sci., v. 27, p. 313–358.

Guarini, J.-M., L, C., and Coston-Guarini, J., 2009, Can the intertidal benthic microalgal primary production account for the "Missing Carbon Sink"? : Journal of Oceanography, Research and Data, v. 1, p. 13-19.

Habicht, K. S., and Canfield, D. E., 1997, Sulfur isotope fractionation during bacterial sulfate reduction in organic-rich sediments: Geochimica et Cosmochimica Acta, v. 61, p. 5351-5361.

Harrison, A. G., and Thode, H. G., 1958, Mechanism of the bacterial reduction of sulphate from isotope fractionation studies: Transactions of the Faraday Society, v. 54, no. 1, p. 84-92.

Horodyski, R. J., Bauld, J., Lipps, J. H., and Mendelson, C. V., 1992, Preservation of prokaryotes and organic-walled and calcareous and siliceous protists, in Schopf, J. W., and Klein, C., eds., The Proterozoic Biosphere: A Multidisciplinary Study, Cambridge University Press, p. 185-193.

Houghton, J. L., Gilhooly, W. P., Kafantaris, F.-C. A., Druschel, G. K., Lu, G.-S., Amend, J. P., Godelitsas, A., and Fike, D. A., 2019, Spatially and temporally variable sulfur cycling in shallow-sea hydrothermal vents, Milos, Greece: Marine Chemistry, v. 208, p. 83-94.

Huerta-Diaz, M. A., Delgadillo-Hinojosa, F., Otero, X. L., Segovia-Zavala, J. A., Hernandez-Ayon, J. M., Galindo-Bect, M. S., and Amaro-Franco, E., 2011, Iron and Trace Metals in Microbial Mats and Underlying Sediments: Results From Guerrero Negro Saltern, Baja California Sur, Mexico: Aquatic Geochemistry, v. 17, p. 603–628.

Jeroschewski, P., Steuckart, C., and Kuhl, M., 1996, An Amperometric Microsensor for the Determination of H_2S in Aquatic Environments: Anal. Chem., v. 68, p. 4351-4357.

Jorgensen, B. B., 1979, A theoretical model of the stable sulfur isotope distribution in marine sediments: Geochimica et Cosmochimica Acta, v. 43, p. 363-374.

Jørgensen, B. B., 1978, A comparison of methods for the quantification of bacterial sulphate reduction in coastal marine sediments: I. Measurements with radiotracer techniques: Geomicrobiol. J., v. 1, p. 11-27.

1073 Kallmeyer, J., Ferdelman, T. G., Weber, A., Fossing, H., and Jørgensen, B. B., 2004, A cold
1074 chromium distillation procedure for radiolabeled sulfide applied to sulfate reduction
1075 measurements. : Limnol. Oceanogr. Methods, v. 2, p. 171-180.
1076
1077 Kamp, A., de Beer, D., Nitsch, J. L., Lavik, G., and Stief, P., 2011, Diatoms respire nitrate to
1078 survive dark and anoxic conditions: Proceedings of the National Academy of Sciences, v. 108, p.
1079 5649-5654.
1080
1081 Kaplan, I. R., and Rittenberg, S. C., 1964, Microbiological fractionation of sulphur isotopes:
1082 Journal of General Microbiology, v. 34, p. 195-212.
1083
1084 Kinsman-Costello, L. E., Sheik, C. S., Sheldon, N. D., Allen Burton, G., Costello, D. M.,
1085 Marcus, D., Uyl, P. A., and Dick, G. J., 2017, Groundwater shapes sediment biogeochemistry
1086 and microbial diversity in a submerged Great Lake sinkhole: Geobiology, v. 15, no. 2, p. 225-
1087 239.
1088
1089 Kjeldsen, K. U., Schreiber, L., Thorup, C. A., Boesen, T., Bjerg, J. T., Yang, T., Dueholm, M. S.,
1090 Larsen, S., Risgaard-Petersen, N., Nierychlo, M., Schmid, M., Bøggild, A., Vossenberg, J. v. d.,
1091 Geelhoed, J. S., Meysman, F. J. R., Wagner, M., Nielsen, P. H., Nielsen, L. P., and Schramm, A.,
1092 2019, On the evolution and physiology of cable bacteria: Proc Natl Acad Sci U S A, v. 116, p.
1093 19116-19125.
1094
1095 Klatt, J. M., Marchant, H., de Beer, D., Ziebis, W., Druschel, G., Medina, M., Chennu, A., and
1096 Dick, G., 2017, Response of Chemotrophic Processes to Dynamic Redox Conditions in a
1097 Cyanobacterial Mat: 27th Goldschmidt Conference, Paris, France, August 2017.
1098
1099 Klatt, J. M., and Polerecky, L., 2015, Assessment of the stoichiometry and efficiency of CO2
1100 fixation coupled to reduced sulfur oxidation: Front. Microbiol., v. 6, p. 484.
1101
1102 Krekeler, D., Teske, A., and Cypionka, H., 1998, Strategies of sulfate-reducing bacteria to
1103 escape oxygen stress in a cyanobacterial mat: FEMS Microbiol Ecol, v. 25, p. 89-96.

Leavitt, W. D., Halevy, I., Bradley, A. S., and Johnston, D. T., 2013, Influence of sulfate reduction rates on the Phanerozoic sulfur isotope record: Proc Natl Acad Sci U S A, v. 110, no. 28, p. 11244-11249.

Lee, C., Love, G. D., Jahnke, L. L., Kubo, M. D., and Des Marais, D. J., 2019, Early diagenetic sequestration of microbial mat lipid biomarkers through covalent binding into insoluble macromolecular organic matter (IMOM) as revealed by sequential chemolysis and catalytic hydropyrolysis: Organic Geochemistry, v. 132, p. 11-22.

Lenton, T. M., and Daines, S. J., 2017, Matworld – the biogeochemical effects of early life on land: New Phytologist v. 215, p. 531–537.

Longphuirt, S., Lim, J.-H., Leynaert, A., Claquin, P., Choy, E.-J., Kang, C.-K., and An, S., 2009, Dissolved inorganic nitrogen uptake by intertidal microphytobenthos: Nutrient concentrations, light availability and migration. : Marine Ecology Progress Series, v. 379, p. 33-34.

Luther, G. W., 2005, Acid volatile sulfide — A comment: Marine Chemistry, v. 97, p. 198-205.

Lyons, T. W., 1997, Sulfur isotopic trends and pathways of iron sulfide formation in upper Holocene sediments of the Black Sea: Geochimica et Cosmochimica Acta, v. 61, p. 3367–3382.

Lyons, T. W., Anbar, A. D., Severmann, S., Scott, C., and Gill, B. C., 2009, Tracking Euxinia in the Ancient Ocean: A Multiproxy Perspective and Proterozoic Case Study: Annu. Rev. Earth Planet. Sci., v. 37, p. 507–534.

Macintyre, H., Geider, R., and Miller, D., 1996, Microphytobenthos: The Ecological Role of the "Secret Garden" of Unvegetated, Shallow-Water Marine Habitats. I. Distribution, Abundance and Primary Production. : Estuaries and Coasts, v. 19, p. 186-201.

Malkin, S. Y., Rao, A. M., Seitaj, D., Vasquez-Cardenas, D., Zetsche, E.-M., Hidalgo-Martinez, S., Boschker, H. T., and Meysman, F. J., 2014, Natural occurrence of microbial sulphur oxidation by long-range electron transport in the seafloor: ISME J, v. 8, p. 1843-1854.

Mandernack, K. W., Krouse, H. R., and Skei, J. M., 2003, A stable sulfur and oxygen isotopic investigation of sulfur cycling in an anoxic marine basin, Framvaren Fjord, Norway: Chemical Geology, v. 195, p. 181–200.

Mariotti, A., Germon, J. C., Hubert, P., Kaiser, P., Leto Ile, R., Tardieux, A., and Tardieux, P., 1981, Experimental determination of nitrogen kinetic isotope fractionation: some principles; illustration for the denitrification and nitrification processes: Pl. Soil, v. 62, p. 413-430.

Merz, E., Dick, G. J., de Beer, D., Grim, S., Hübener, T., Littmann, S., Olsen, K., Stuart, D., Lavik, G., Marchant, H. K., and Klatt, J. M., 2020, Nitrate respiration and diel migration patterns of diatoms are linked in sediments underneath a microbial mat: Environ Microbiol, p. https://doi.org/10.1111/1462-2920.15345.

Meyer, N. R., Zerkle, A. L., and Fike, D. A., 2017, Sulphur cycling in a Neoarchaean microbial mat: Geobiology, v. 15, no. 3, p. 353-365.

Nakai, N., and Jensen, M. L., 1964, The kinetic isotope effect in the bacterial reduction and oxidation of sulfur: Geochimica et Cosmochimica Acta, v. 28, p. 1893-1912.

Nielsen, L. P., Risgaard-Petersen, N., Fossing, H., Christensen, P. B., and Sayama, M., 2010, Electric currents couple spatially separated biogeochemical processes in marine sediment: Nature, v. 463, p. 10.1038/nature08790.

Nold, S. C., Bellecourt, M. J., Kendall, S. T., Ruberg, S. A., Sanders, T. G., Klump, J. V., and Biddanda, B. A., 2013, Underwater sinkhole sediments sequester Lake Huron's carbon: Biogeochemistry, v. 115, p. 235–250.

Nold, S. C., Pangborn, J. B., Zajack, H. A., Kendall, S. T., Rediske, R. R., and Biddanda, B. A., 2010a, Benthic bacterial diversity in submerged sinkhole ecosystems. Applied and Environmental Microbiology: Environmental Microbiology, v. 76, p. 347–351.

Nold, S. C., Zajack, H. A., and Biddanda, B. A., 2010b, Eukaryal and Archaeal Diversity in a Submerged Sinkhole Ecosystem Influenced by Sulfur-Rich, Hypoxic Groundwater: Journal of Great Lakes Research, v. 36, p. 366-375.

Pasquier, V., Sansjofre, P., Rabineau, M., Revillon, S., Houghton, J., and Fike, D. A., 2017, Pyrite sulfur isotopes reveal glacial-interglacial environmental changes: Proc Natl Acad Sci U S A, v. 114, no. 23, p. 5941-5945.

Pellerin, A., Antler, G., Holm, S. A., Findlay, A. J., Crockford, P. W., Turchyn, A. V., Jørgensen, B. B., and Finster, K., 2019, Large sulfur isotope fractionation by bacterial sulfide oxidation: Science Advances, v. 5, p. eaaw1480.

Peters, S. E., Husson, J. M., and Wilcots, J., 2017, The rise and fall of stromatolites in shallow marine environments: Geology, v. 45, no. 6, p. 487-490.

Pfeffer, C., Larsen, S., Song, J., Dong, M., Besenbacher, F., Meyer, R. L., Kjeldsen, K. U., Schreiber, L., Gorby, Y. A., El-Naggar, M. Y., Leung, K. M., Schramm, A., Risgaard-Petersen, N., and Nielsen, L. P., 2012, Filamentous bacteria transport electrons over centimetre distances: Nature, v. 491, p. 218-221.

Picard, A., Gartman, A., Clarke, D. R., and Girguis, P. R., 2018, Sulfate-reducing bacteria influence the nucleation and growth of mackinawite and greigite: Geochimica et Cosmochimica Acta, v. 220, p. 367-384.

Pinckney, J., and Zingmark, R. G., 1991, Effects of tidal stage and sun angles on intertidal benthic microalgal productivity: Marine Ecology Progress Series, v. 76, p. 81-89.

Present, T. M., Trower, L., Stein, N., Alleon, J., Bahniuk, A., Gomes, M. L., Lingappa, U., Metcalfe, K., Orzechowski, E. A., Riedman, L. A., Sanders, C. B., Morris, D. K., O'Reilly, S., Sibert, E. C., Thorpe, M., Tarika, M., Fischer, W. W., Knoll, A. H., and Grotzinger, J. P., 2018, Sedimentology and Geochemistry of Ooid Sands Buried Beneath Microbial Mats, Little Ambergris Cay, Turks and Caicos Islands. : American Association of Petroleum Geologists Annual Convention & Exhibition.

Raven, M. R., Sessions, A. L., Fischer, W. W., and Adkins, J. F., 2016, Sedimentary pyrite d34S differs from porewater sulfide in Santa Barbara Basin: Proposed role of organic sulfur: Geochimica et Cosmochimica Acta, v. 186, p. 120-134.

Revsbech, N. P., 1989, An oxygen microsensor with a guard cathode: Limnology and Oceanography, v. 34, p. 474-478.

Revsbech, N. P., Jorgensen, B. B., Blackburn, T. H., and Cohen, Y., 1983, Microelectrode studies of the photosynthesis and 02, H&5, and pH profiles of a microbial mat1: Limnol. Oceanogr., v. 26, p. 1062-1074.

Rickard, D., Butler, I. B., and Oldroyd, A., 2001, A novel iron sulphide mineral switch and its implications for Earth and planetary science: Earth and Planetary Science Letters, v. 189, p. 85-91.

Rickard, D., Grimes, S., Butler, I., Oldroyd, A., and Davies, K. L., 2007, Botanical constraints on pyrite formation: Chemical Geology, v. 236, p. 228-246.

Rickard, D., and Luther, G. W., 2007, Chemistry of Iron Sulfides: Chem. Rev., v. 107, p. 514−562.

Rickard, D., and Morse, J. W., 2005, Acid volatile sulfide (AVS): Marine Chemistry, v. 97, p. 141-197.

Rickard, D. T., 1975, Kinetics and mechanism of pyrite formation at low temperatures: Amer. J. Sci., v. 275, p. 636-652.

Rickard, D. T., 1997, Kinetics of pyrite formation by the H2S oxidation of iron (II) monosulfide in aqueous solutions between 25 and 125°C: The rate equation: Geochimica et Cosmochimica Acta, v. 61, p. 115-134.

Rickard, D. T., 2012, Sulfidic Sediments and Sedimentary Rocks, Oxford, Elsevier.

Rickard, D. T., and Luther, G. W., 1997, Kinetics of pyrite formation by the H2S oxidation of iron (II) monosulfide in aqueous solutions between 25 and 125°C: The mechanism: Geochimica et Cosmochimica Acta, v. 61, p. 135-147.

Rickard, D. T., Oldroyd, A., and Cramp, A., 1999, Voltammetric Evidence for Soluble FeS Complexes in Anoxic Estuarine Muds: Estuaries, v. 22, p. 693-701.

Rico, K. I., and Sheldon, N. D., 2019, Nutrient and iron cycling in a modern analogue for the redoxcline of a Proterozoic ocean shelf: Chemical Geology, v. 511, p. 42-50.

Rico, K. I., Sheldon, N. D., Gallagher, T. M., and Chappaz, A., 2019, Redox chemistry and molybdenum burial in a Mesoproterozoic Lake. : Geophysical Research Letters, v. 46, p. 5871–5878.

Rico, K. I., Sheldon, N. D., and Kinsman-Costello, L. E., 2020, Associations between redox-sensitive trace metals and microbial communities in a Proterozoic ocean analogue: Geobiology, v. 18, p. 462–475.

Riding, R., 2006, Microbial carbonate abundance compared with fluctuations in metazoan diversity over geological time: Sedimentary Geology, v. 185, p. 229-238.

Round, F. E., and Palmer, J. D., 1966, Persistent, vertical-migration rhythms in benthic microflora.: II. Field and laboratory studies on diatoms from the banks of the river avon: Journal of the Marine Biological Association of the United Kingdom, v. 46, p. 191-214.

Ruberg, S. A., Kendall, S. T., Biddanda, B. A., Black, T., Nold, S. C., Lusardi, W. R., Green, R., Casserley, T., Smith, E., Sanders, T. G., Lang, G. A., and Constant, S. A., 2008, Observations of the Middle Island Sinkhole in Lake Huron – A unique hydrogeologic and glacial creation of 400 million years: Marine Technology Society Journal, v. 42, p. 12–21.

Schoonen, M. A. A., and Barnes, H. L., 1991, Reactions forming pyrite and marcasite from solution: I. Nucleation of FeS2 below 100°: Geochimica et Cosmochimica Acta, v. 55, p. 1495-1504.

Schwedt, A., Kreutzmann, A. C., Polerecky, L., and Schulz-Vogt, H. N., 2012, Sulfur respiration in a marine chemolithoautotrophic beggiatoa strain: Front Microbiol, v. 2, p. 276.

Seitaj, D., Schauer, R., Sulu-Gambari, F., Hidalgo-Martinez, S., Malkin, S. Y., Burdorf, L. D. W., Slomp, C. P., and Meysman, F. J. R., 2015, Cable bacteria generate a firewall against euxinia in seasonally hypoxic basins: Proc Natl Acad Sci U S A, v. 112, p. 13278-13283.

Sharrar, A. M., Flood, B. E., Bailey, J. V., Jones, D. S., Biddanda, B. A., Ruberg, S. A., Marcus, D. N., and Dick, G. J., 2017, Novel Large Sulfur Bacteria in the Metagenomes of Groundwater-Fed Chemosynthetic Microbial Mats in the Lake Huron Basin: Front Microbiol, v. 8, p. 791.

Sim, M. S., Bosak, T., and Ono, S., 2011, Large Sulfur Isotope Fractionation Does Not Require Disproportionation: Science, v. 333, no. 6038, p. 74-77.

Snider, M. J., Biddanda, B. A., Lindback, M., Grim, S. L., and Dick, G. J., 2017, Versatile photophysiology of compositionally similar cyanobacterial mat communities inhabiting submerged sinkholes of Lake Huron: Aquatic Microbial Ecology, v. 79, p. 63-78.

Taylor, B. E., Wheeler, M. C., and Nordstrom, D. K., 1984, Isotope composition of sulphate in acid mine drainage as measure of bacterial oxidation: Nature, v. 308, p. 538-541.

Thiel, J., Byrne, J. M., Kappler, A., Schink, B., and Pester, M., 2019, Pyrite formation from FeS and H2S is mediated through microbial redox activity: Proc Natl Acad Sci U S A, v. 116, p. 6897-6902.

Voorhies, A. A., Biddanda, B. A., Kendall, S. T., Jain, S., Marcus, D. N., Nold, S. C., Sheldon, N. D., and Dick, G. J., 2012, Cyanobacterial life at low O2: Community genomics and function reveal metabolic versatility and extremely low diversity in a Great Lakes sinkhole mat: Geobiology, v. 10, p. 250–267.

Voorhies, A. A., Eisenlord, S. D., Marcus, D. N., Duhaime, M. B., Biddanda, B. A., Cavalcoli, J. D., and Dick, G. J., 2016, Ecological and genetic interactions between cyanobacteria and viruses in a low-oxygen mat community inferred through metagenomics and metatranscriptomics: Environ Microbiol, v. 18, no. 2, p. 358-371.

Wacey, D., McLoughlin, N., Whitehouse, M. J., and Kilburn, M. R., 2010, Two coexisting sulfur metabolisms in a ca. 3400 Ma sandstone: Geology, v. 38, p. 1115-1118.

Walter, M. R., 1976, Hot-spring sediments in Yellowstone National Park, in Walter, M. R., ed., Stromatolites: New York, Elsevier, p. 489-498.

Zerkle, A. L., Farquhar, J., Johnston, D. T., Cox, R. P., and Canfield, D. E., 2009, Fractionation of multiple sulfur isotopes during phototrophic oxidation of sulfide and elemental sulfur by a green sulfur bacterium: Geochimica et Cosmochimica Acta, v. 73, no. 2, p. 291-306.

Zerkle, A.L., Jones, D.S., Farquhar, J. and Macalady, J.L. (2016) Sulfur isotope values in the sulfidic Frasassi cave system, central Italy: A case study of a chemolithotrophic S-based ecosystem. Geochimica et Cosmochimica Acta 173, 373-386.

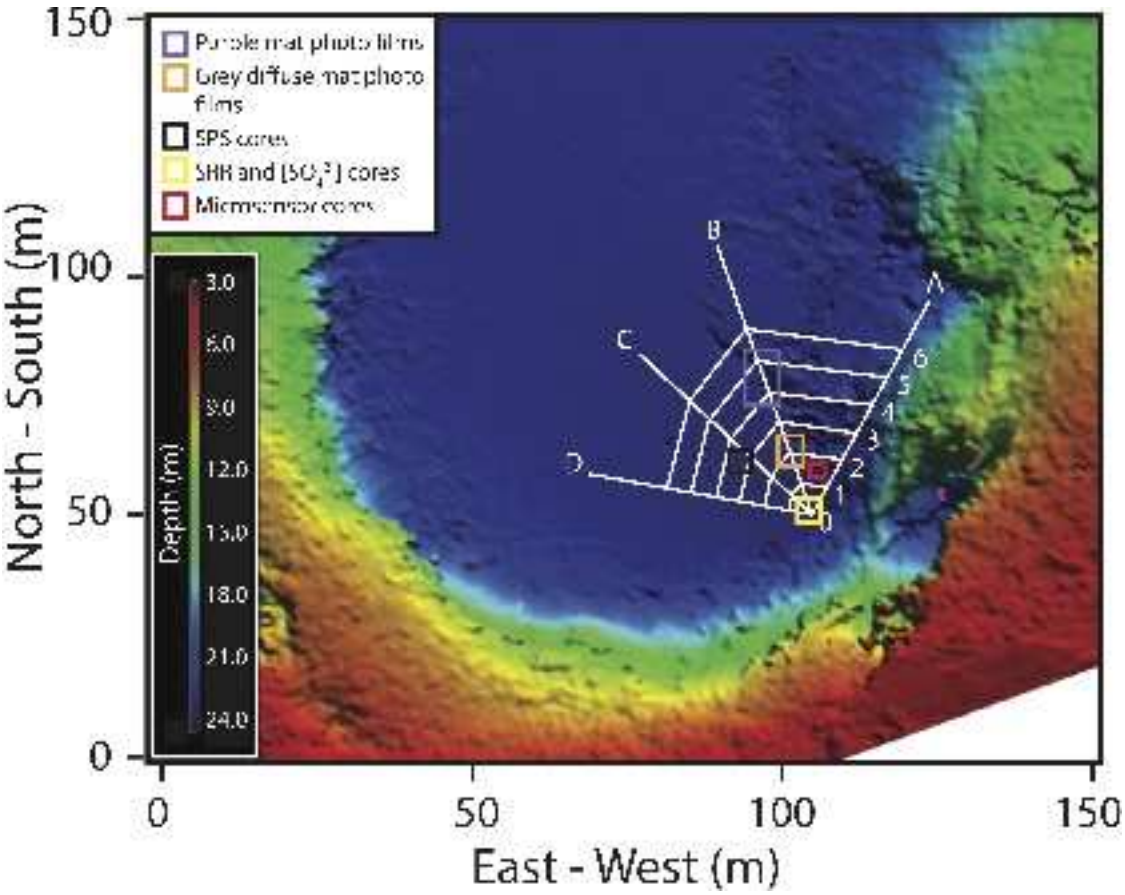

gbi_12466_f1.jpg

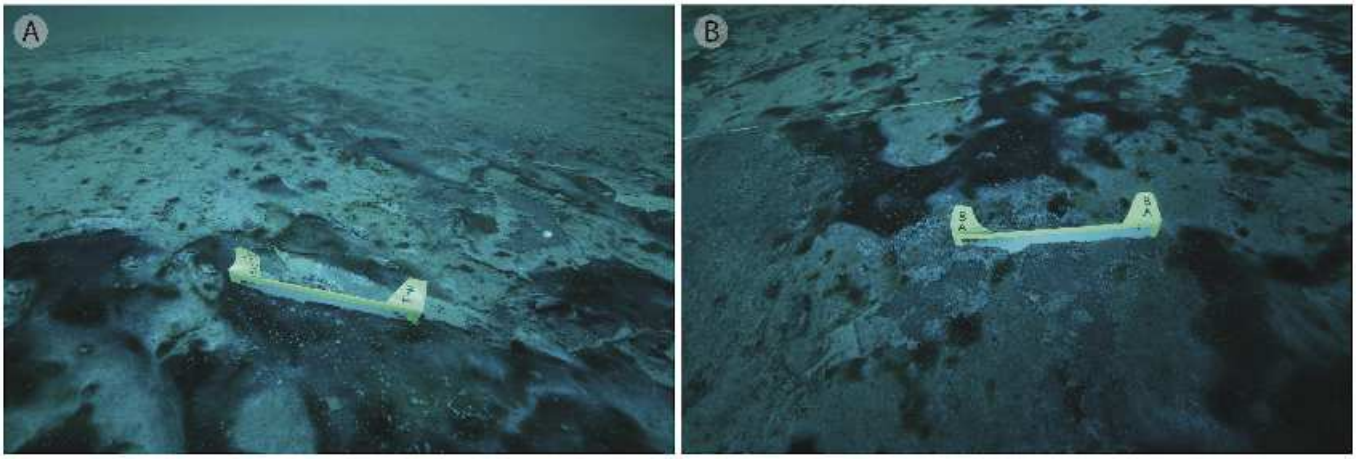

gbi_12466_f2.png

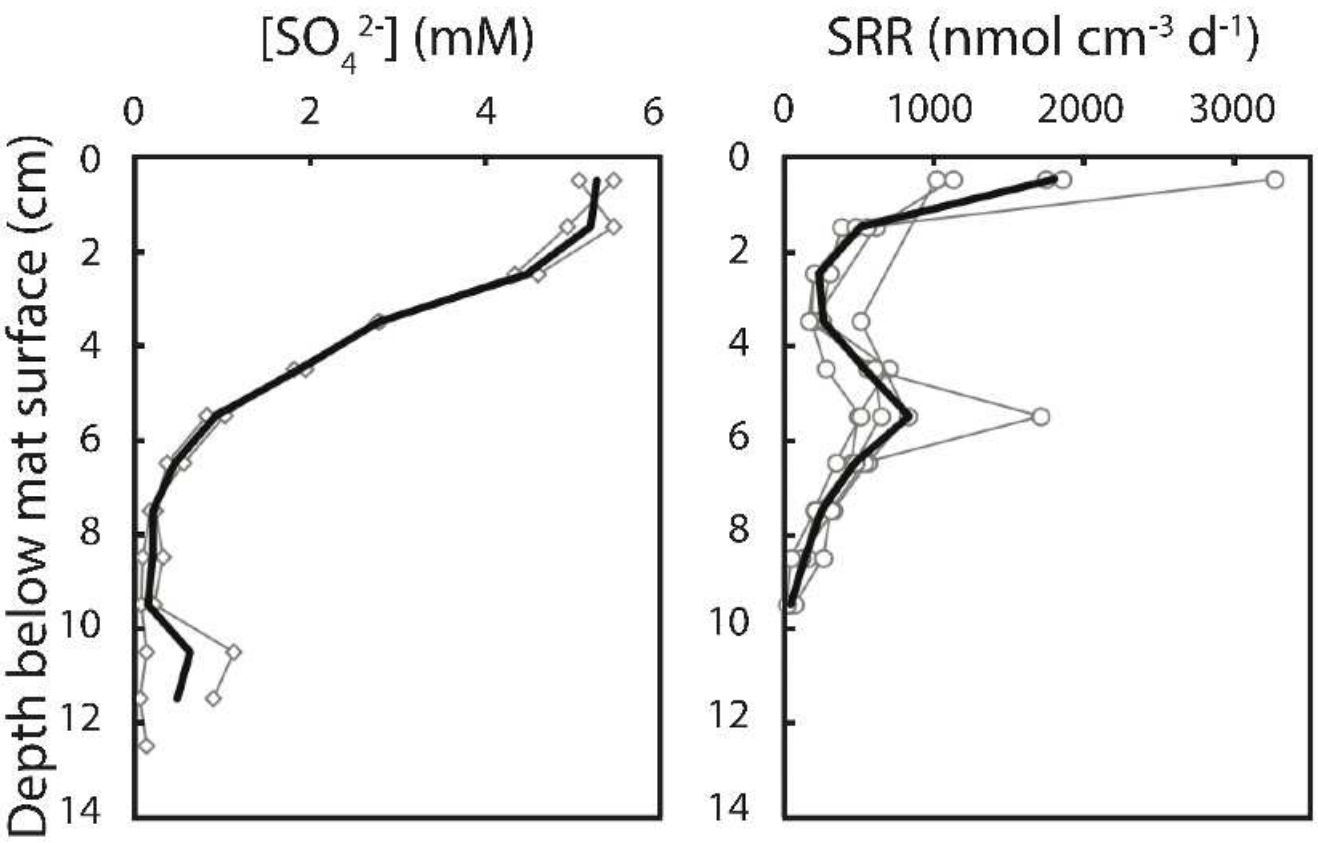

gbi_12466_f3.png

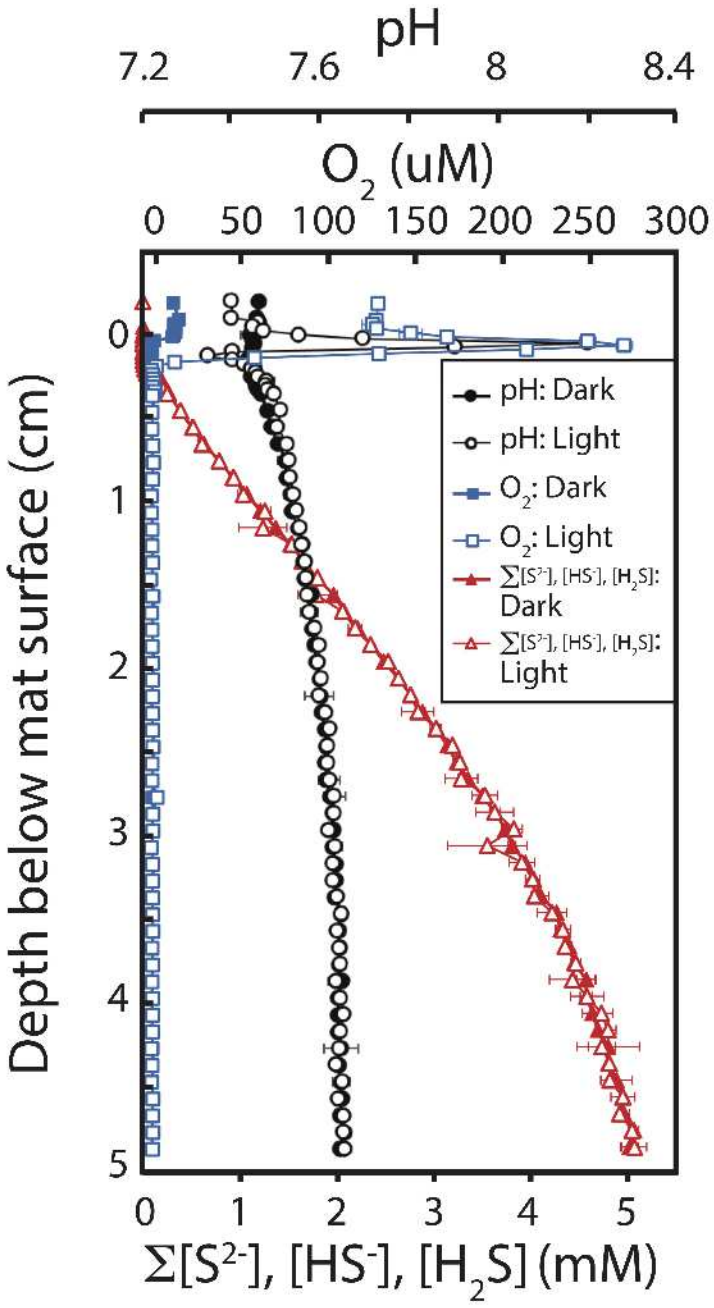

gbi_12466_f4.jpg

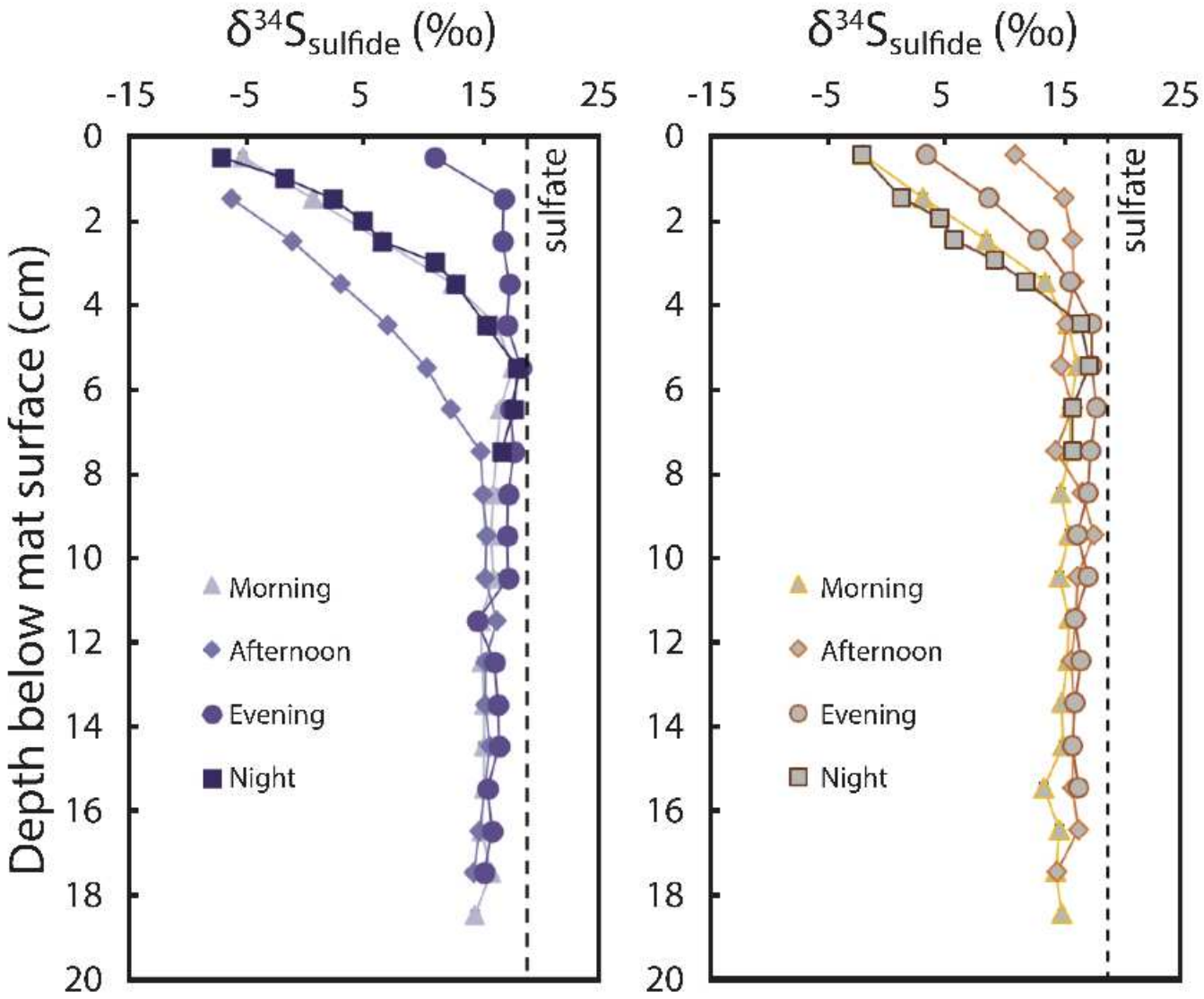

gbi_12466_f5.jpg

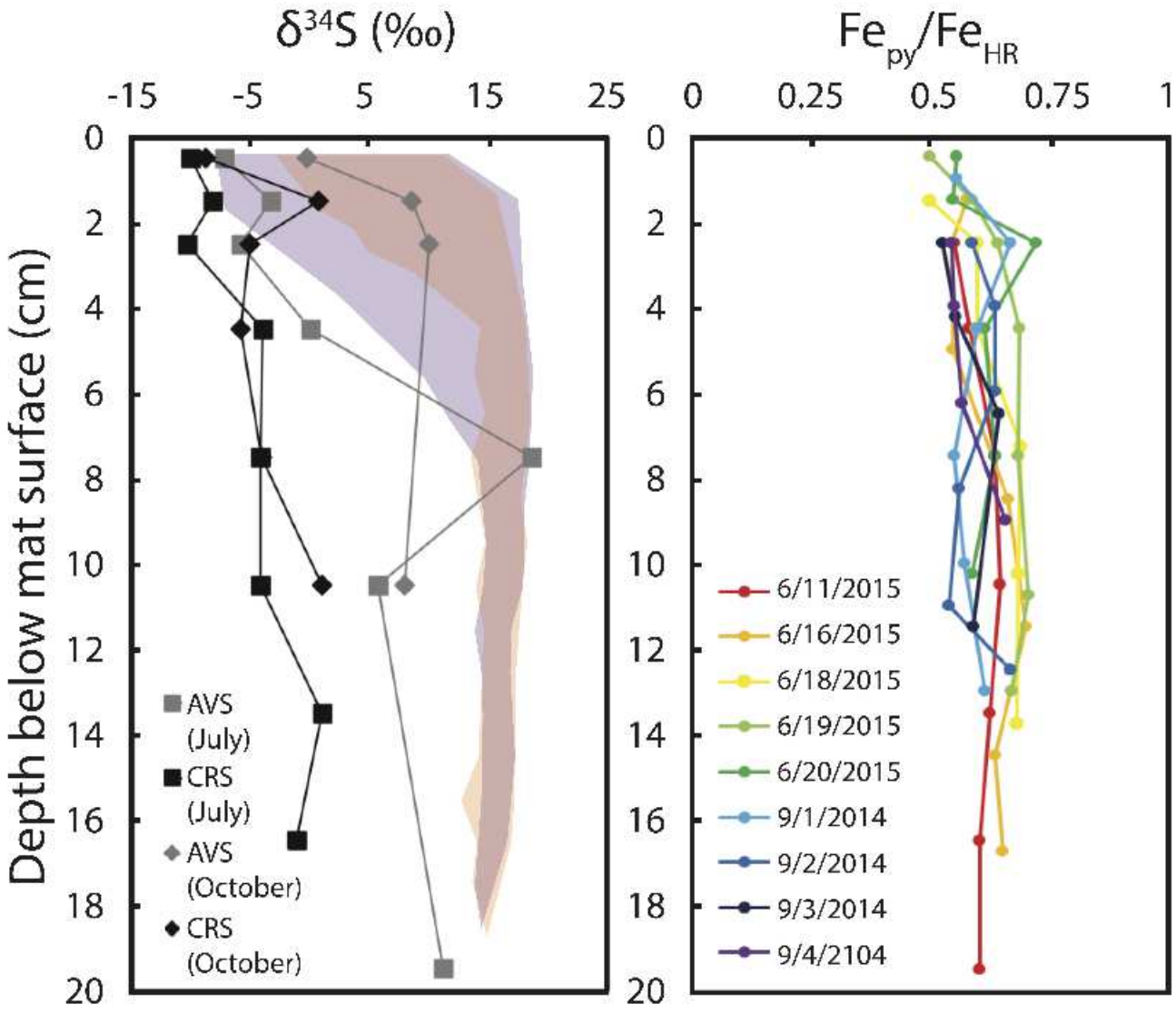

gbi_12466_f6.jpg

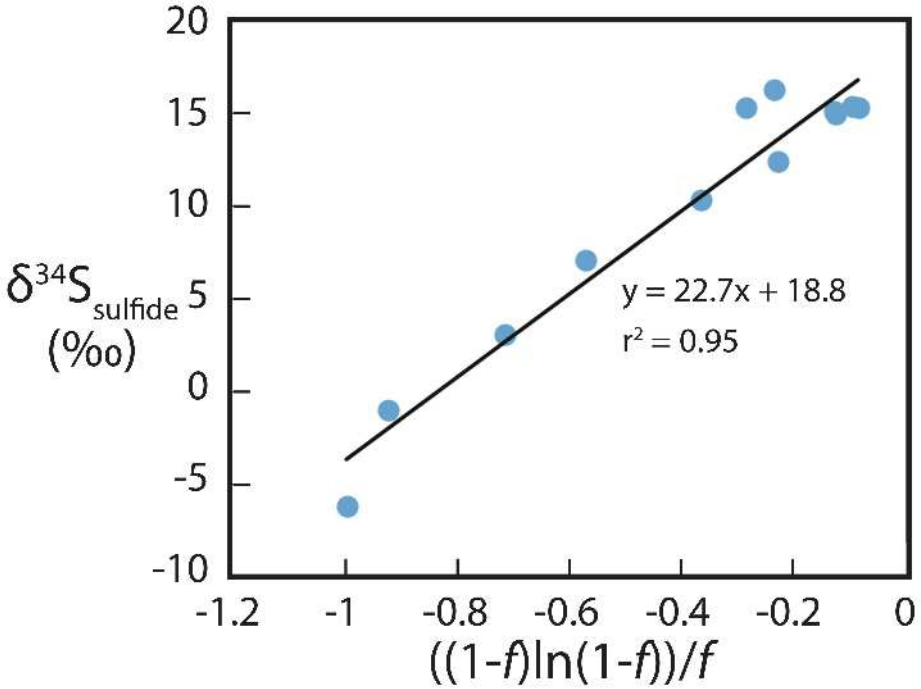

gbi_12466_f7.jpg

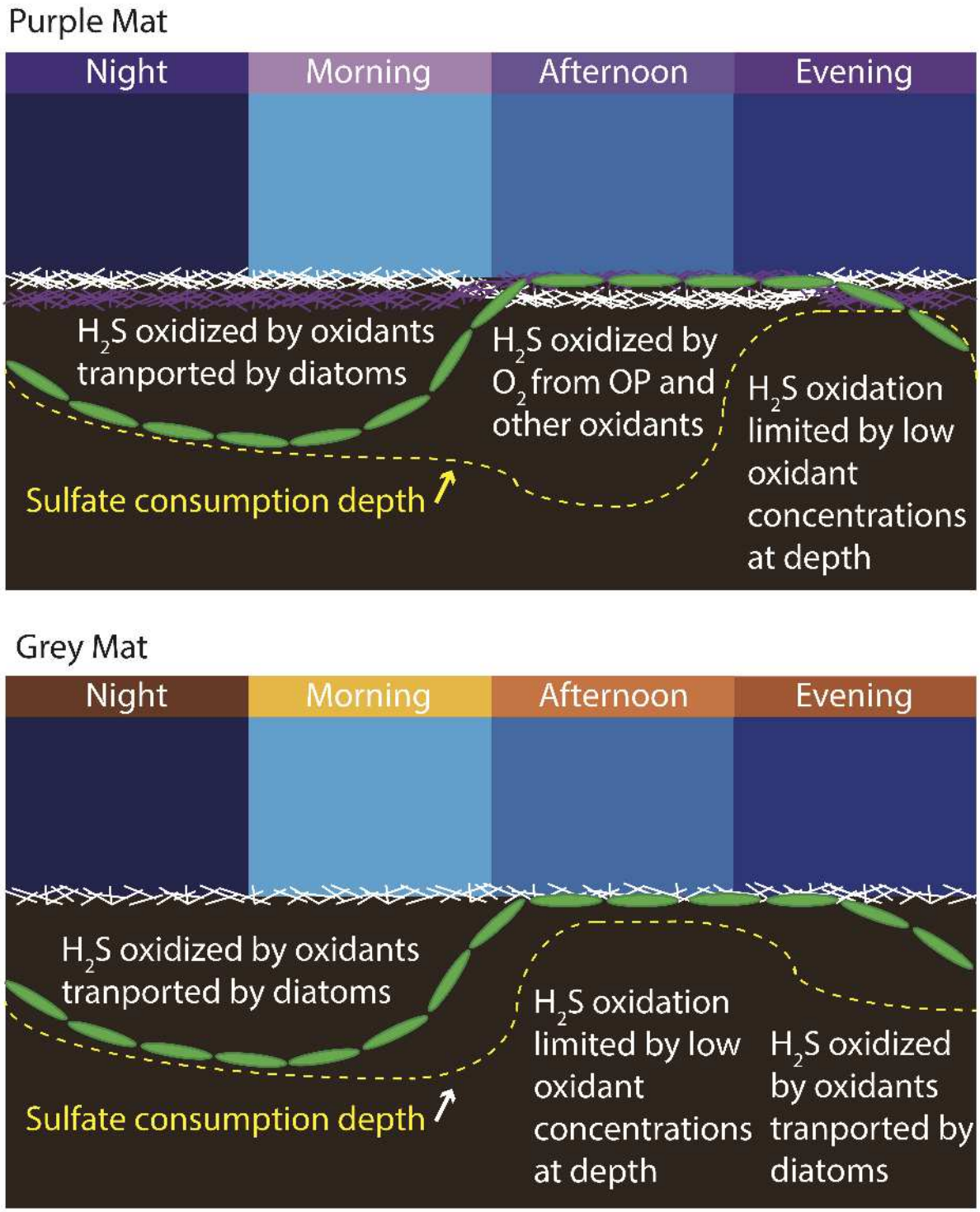

gbi_12466_f8.jpg